Photocatalytic oxidation of MEK over hierarchical TiO$_2$ catalysts: Effect of photocatalyst features and operating conditions

Alireza Haghighat Mamaghani, Fariborz Haghighat*, Chang-Seo Lee

Department of Building, Civil and Environmental Engineering, Concordia University, Montreal, Canada

ABSTRACT

A novel hydrothermal route was developed to synthesize crystalline and hierarchically porous TiO$_2$ at mild conditions under acidic/basic reaction environments. A good control over the key features of catalysts could be achieved by varying the pH of the starting solution (pH = 2–12) and type of acid during preparation. Crystalline, textural, and optical properties of photocatalysts were characterized in order to explore the connections between catalysts' features and photoactivity. The activities of catalysts were evaluated for decomposition of methyl ethyl ketone (MEK) in a continuous flow photoreactor. To gain insight into the impact of main operating conditions on photocatalytic oxidation (PCO) processes, experiments were conducted at wide ranges of inlet concentration, relative humidity, and residence time. X-ray diffraction (XRD) and transmission electron microscopy (TEM) confirmed that yielded titania samples possess good crystallinity and mainly consist of anatase polymorph. Results of X-ray photoelectron spectroscopy (XPS) indicated that the population of hydroxyl groups on the surface of TiO$_2$ declines as the acidity of hydrothermal solution increases. Hierarchical porous structure with ultra-long parallel macrochannels and large macropores ($> 0.5\,\mu m$) could be directly observed in scanning electron microscopy (SEM). The multimodal porous structure offers higher light utilization, enhanced mass transport, and superior adsorption capacity for air pollutants. Photoluminescence spectroscopy revealed that the enhancement in crystallinity has an impact on the separation of photo-induced charge carriers. Moreover, a satisfactory linear correlation between the ability of photocatalysts to generate ·OH and crystallinity could be found. Under the harshest operating condition (residence time = 0.012 s, relative humidity = 50%, concentration = 1000 ppb), the TiO$_2$ synthesized in nitric acid (pH = 4) achieved the highest MEK removal efficiency, 36.9%, which substantially surpassed that of P25, 14.5%. Hierarchical porosity, optimum trade-off between surface area and crystallinity, existence of meso- and macropores, small crystal size, and high ·OH generation ability could account for the superior performance. A tentative reaction pathway for MEK photo-degradation and a health-risk index were put forward considering the by-products detected in the gas phase.

1. Introduction

Semiconductor-mediated photocatalytic oxidation (PCO) has been proven to be an efficient and viable technology for air remediation [1,2]. A fundamental process in PCO is the excitation of electrons, from the valence band to the conduction band, which gives rise to generation of charge carriers (electron (e$^-$) and hole (h$^+$)). In order for excitation to occur, electrons need to be illuminated by an appropriate light source which emits photons with energy equal to or greater than semiconductor's band gap. A part of generated charge carriers will be lost due to bulk and surface recombinations, while the others migrate to the surface and react with adsorbed water, surface hydroxyl groups, and

oxygen and produce reactive species such as hydroxyl radical. A series of chemical reactions eventually result in the decomposition of pollutant molecules adsorbed on the surface to CO$_2$, H$_2$O and unwanted by-products [3].

In the past three decades, TiO$_2$-based materials have attracted much research interest in PCO of air and water pollutants [4–8]. TiO$_2$ key properties including crystallinity, crystalline phase, surface area, crystal size, porosity, density of surface hydroxyl groups, exposed facet, and surface acidity have been shown to significantly affect the photocatalytic activity. Engineering of Ti-based nanomaterials characteristics and morphology has been investigated using various preparation routes including sol-gel, hydrothermal, solvothermal, electrodeposition, vapor

deposition, microwave, flame technique, etc [9–11]. Among these strategies, hydrothermal synthesis has demonstrated the ability of producing large-surface-area, porous, and crystalline titanium dioxide. In hydrothermal route, chemical reactions take place in aqueous media under autogenous pressure and temperatures usually lower than 250 °C [12]. Synergetic effect of high temperature and pressure, and water-catalysis facilitates the transformation of amorphous TiO_2 to crystalline form. Moreover, a large number of experimental conditions including hydrothermal time, temperature, pressure, pH, type of acid/base, and type of solvent enable good control over the properties of final product.

Research on hierarchical catalysts has exponentially increased during the past 10 years in areas of environmental purification, hydrogen generation, and CO_2 reduction [13]. Hierarchy is a property with numerous examples in nature, society, and human body. Hierarchical structure of roots and leaves of trees, river deltas, nervous system, and human lung and blood circuit are very familiar instances of hierarchy around us. A material can be considered hierarchical if it has structural elements of different length scales, each of which with a specific function [14,15]. Hierarchical photocatalysts benefit from a number of advantages including: accessible and intertwined networks of pores, large surface area, more exposed active sites, improved light harvesting, and better mass transport. Synthesis of multimodal hierarchical photocatalysts has been the focus of numerous works due to the fact that such architectures can render the high surface area of micro-/mesoporous materials and also the enhanced mass transfer of macroporous solids [14–16]. The most convenient method to prepare hierarchically porous materials at the desired length scales is templating strategy [17,18]. Although templating strategies are uniquely efficient for fabricating multimodal porous catalysts, they are also expensive, ungreen, and demanding in terms of required materials and labor. Moreover, during template removal by calcination or dissolution inevitable structural changes occur which could adversely affect the porous hierarchy and surface area [19,20]. Consequently, template-free synthesis approaches are highly sought after since they could be far cheaper, more environmentally-friendly, and easier to scale-up.

Table 1 lists the previous works in the literature on photocatalytic oxidation of MEK over titanium dioxide. Photocatalyst preparation and coating method, type of reactor, main operating conditions, and maximum achieved MEK removal efficiency are presented to allow easier comparison between the existing studies. The point that is of particular importance is that in most of these studies, the performance of the PCO system was determined at unrealistic operating conditions: high MEK concentration, low humidity, long residence time, and/or high light intensity.

In the present study, we employed a template-free hydrothermal method to synthesize crystalline and meso-/macroporous TiO_2 photocatalysts. The impact of pH value of the hydrothermal solution and the type of acid/base on physical and chemical features and morphology of yielded titania were examined. Photocatalysts were characterized by XRD, nitrogen adsorption-desorption, XPS, SEM, TEM, photoluminescence spectroscopy, and Fourier transform infrared (FTIR). Accordingly, the dependence of photocatalyst crystallinity, crystal phase and size, surface area, porosity, OH groups population, morphology, and e^--h^+ recombination rate on preparation factors were discussed. As shown in Table 1, there are only a few studies on photocatalytic oxidation of methyl ethyl ketone in air; therefore, the performance, by-products, reaction mechanism, and health aspects of MEK degradation over titania are not fully investigated. To assess the performance of developed TiO_2 catalysts in this work, photocatalytic oxidation of MEK under realistic operating conditions (e.g. pollutant concentration, relative humidity, and residence time) was performed. The obtained photocatalytic activities were justified by underlining the role of key characteristics of photocatalysts in each step of heterogeneous photocatalysis. Furthermore, the influence of operating conditions on MEK removal efficiency, by-products generation, and health-risk index were examined. These findings are hoped to deepen our

Table 1
MEK photocatalytic oxidation tests in the literature.

Photocatalyst	Photocatalyst preparation route	Coating method/ Photocatalyst loading (mg/cm²)	Support material	Reactor type	C (ppm)	RH (%)	t (s)	Light source /I (W/m²)	η (%)	Major limitations	Ref.
P25	–	–/0.25	Glass-slide	Batch reactor	2033.9	30	–	Mercury lamp, λ_{max} = 365 nm/-	50 (after 250 min)	High MEK concentration; batch process	[21]
P25, UV100	–	Coated on internal side of the Pyrex tube/1.3	–	Single pass annular Pyrex reactor	1500	50	10.3	Blacklight, λ_{max} = 380 nm/33	39 (P25) 72 (UV100)	High MEK concentration; long residence time	[22]
P25	–	Dip coating/0.2 (gTiO₂/gAl₂O₃)	γ -Al₂O₃	Fluidized bed reactor	800	45	–	UVC lamp, λ_{max} = 254 nm/-	75	High MEK concentration; reactor type	[23]
F/P-TiO₂	Ionic liquid assisted sol-gel	Pipetting technique/ 1	Glass-plate	Single-pass continuous gas flow reactor	100	50	7.5	UVA blacklight lamp, λ_{max} = 365 nm/ 30	56	High MEK concentration; long residence time	[24]
P25	–	–	–	Annular fluidized bed photoreactor	20.31	60	1.41	UVC lamp, λ_{max} = 254 nm/-	42	High MEK concentration; reactor type	[25]
N-modified titania nanotubes	Hydrothermal	Coated on internal side of the Pyrex tube/1.67	–	Single pass annular Pyrex reactor	500	50	–	UVA blacklight lamp, λ_{max} = 365 nm/ 45.3	8	High MEK concentration; long residence time	[26]
Mesoporous TiO₂	Surfactant assisted sol-gel	Dip coating	Glass-slide	Batch reactor	22.7	< 3	–	UVA lamp, λ_{max} = 365 nm/-	100 (after 50 min)	High MEK concentration; batch process; low humidity	[27]
PC500, P25, PC50	–	–	Glass beads	Fluidized bed reactor	250	8	–	UVA-LED, λ_{max} = 365 nm/900	85 (PC500) 79 (P25) 64 (PC50)	High MEK concentration; reactor type; high light intensity	[28]

C: MEK inlet or initial concentration; RH: relative humidity; t: residence time; I: light intensity; η: removal efficiency.

Table 2
Hydrothermal reaction medium of TiO$_2$ photocatalysts.

Name	Reaction medium	Solution pH	Acid/base concentration (mol/L)
H-SA2	Sulfuric acid (H$_2$SO$_4$)	2	0.01
H-SA4		4	0.0001
H-NA2	Nitric acid (HNO$_3$)	2	0.01
H-NA4		4	0.0001
H-HCA2	Hydrochloric acid (HCl)	2	0.01
H-HCA4		4	0.0001
H-FA2	Formic acid (HCOOH)	2	0.5
H-FA4		4	0.00015
H-AA2	Acetic acid (CH$_3$COOH)	2	5
H-AA4		4	0.0006
H-Base	Pure water	6	–
H-A10	Ammonium hydroxide	10	0.0007
H-A12		12	6

understandings of the complex interplay between photocatalyst properties and its performance in air purification.

2. Experimental

2.1. Materials and photocatalyst preparation

Titanium (IV) butoxide (Ti(OC$_4$H$_9$)$_4$,TBOT) and terephthalic acid (TA) were purchased from Sigma-Aldrich and used without further purification. HCl (36.5 wt %), NH$_4$OH (30 wt %), H$_2$SO$_4$ (98 wt %), HNO$_3$ (70 wt %), acetic acid (97 wt %), formic acid (88 wt %), and MEK (≥99%) were purchased from Fischer. Commercial P25 from Evonik has been utilized as reference photocatalyst.

In a typical synthesis procedure, a specific volume of TBOT was added slowly (~2 ml/min) to an aqueous solution (containing acid/base with the desired molarity and pH, Table 2) in a 250 ml beaker without stirring. The volume ratio of the aqueous solution to TBOT in all experiments was kept at 10.4. After aging for 24 h at ambient temperature (21 °C), the mixture and the formed precipitates were carefully transferred to a 100 ml Teflon-lined stainless steel autoclave. The autoclave filling was approximately 80% in the preparation of all samples. Subsequently, the autoclave was heated at a rate of 3 °C/min to 180 °C in an air oven and maintained at that temperature for 12 h. At this temperature, the autogeneous pressure within the reactor (resulted from water vapor pressure) is approximately 1 MPa; however, it is noteworthy that the actual pressure should be slightly higher due to CO$_2$ evolution via decomposition of titanium precursor [29]. Then, the reactor was cooled down to room temperature at rate of -3 °C/min. After hydrothermal reaction, the solution was filtered and the precipitates were washed several times with distilled water until the washing solution reached pH of ca. 6. The resulting white-yellow solids were dried at 100 °C for 12 h to remove water and obtain the final titania samples for characterization and performance evaluation. The properties of aqueous solution during hydrothermal preparation and the assigned name to each photocatalyst are given in Table 2.

In order to verify the repeatability of the preparation protocol, three different batches of H-Base catalyst were synthesized following the exact same procedure and subsequently characterized (Table S1). The characterization results indicated small variations in surface area, crystallinity, crystal size, and anatase content among these samples. This observation confirms that the applied synthesis technique offers a good degree of repeatability.

2.2. Photocatalyst characterization

Degree of crystallinity, phase composition, and crystal size were studied by X-ray diffraction (Bruker, D8 advance). The average crystal size of each titania polymorph was calculated by Scherrer equation using the diffraction peaks corresponding to anatase (101) plane and brookite (121) plane. The phase composition was estimated from the integrated intensities of anatase (101) and brookite (121) peaks. The surface morphology was investigated by scanning electron microscope (SEM, Hitachi S-4700 Model). Transmission electron microscopy (TEM) and high-resolution TEM (HR-TEM) images were collected using a FEI Tecnai TF-20 S/TEM instrument. The Brunauer-Emmett-Teller surface areas (S$_{BET}$) and N$_2$ adsorption-desorption isotherms of photocatalysts were analyzed by a nitrogen adsorption apparatus (AUTOSORB-1, Quantrochrome Instruments Co.). The S$_{BET}$ was assessed by multipoint BET method using the adsorption data in the relative pressure (p/p$_0$) range 0.05-0.3. The pore size distributions were determined from desorption branches of isotherms by the Density Functional Theory (DFT). FTIR analyses were carried out with a Nicolet 6700 FT-IR spectrometer (Thermo Fisher Scientific). Spectra were recorded in the range of 4000–600 cm^{-1} at a resolution of 4 cm^{-1} and an absorbance detection limit of 0.001 a.u. Titania powders were degassed at 80 °C for 12 h prior to the FTIR analysis in a vacuum oven. Surface chemical compositions of photocatalysts were investigated using an X-ray Photoelectron Spectroscopy (XPS) (Thermo Scientific K-Alpha spectrometer, USA) equipped with an Al Kα excitation source and X-ray spot size of 200 μm in diameter. All the binding energies were referenced to the C 1s peak at 284.6 eV of the surface adventitious carbon. In order to study the recombination of charge carriers in photocatalysts, the photoluminescence emission spectra (PL) were measured on a PerkinElmer LS45 Fluorescence spectrometer. The excitation wavelength and the scanning speed were 300 nm and 500 nm/min, respectively, and the width of excitation and emission slits were 10.0 nm. To determine ·OH concentration on the surface of UV-illuminated TiO$_2$, photoluminescence method (using fluorescence spectrophotometer; Varian Cary Eclipse, Agilent) with terephthalic acid as the probe molecule was utilized (details presented in the supplementary material).

2.3. Photocatalytic activity and health-risk measurements

The photocatalytic activity was evaluated in a small-scale continuous flow photoreactor by decomposition of MEK in air. A scheme of the test-rig along with the details of experimental setup and operation, and analytical methods are provided in the supplementary material. Table 3 lists the operating parameters used during MEK photocatalytic oxidation experiments.

Photocatalysts performances are compared in terms of total MEK removal efficiency, amount of generated by-products in the gas phase, and health-risk index.

MEK single-pass removal efficiency and by-products generation are defined as follows:

$$\text{Single-pass removal efficiency}, \eta(\%) = \frac{(C^{in} - C^{out})}{C^{in}} \times 100 \quad (1)$$

where C^{in} and C^{out} are the upstream and downstream concentrations of MEK in ppb, respectively.

$$\text{By-product generation}, G_i(ppb) = C_{i,out} - C_{i,in} \quad (2)$$

Table 3
Photocatalysis experimental conditions.

Parameter	Value	Unit
Inlet concentration	101.8 ± 5.4, 504.7 ± 11.6, 1010 ± 29.8	ppb
Relative humidity	0, 19.9 ± 0.97, 48.7 ± 1.39	%
Volumetric flow rate	20, 30, 50	L/min
Residence time	0.012, 0.02, 0.03	s
Light intensity	5	mW/cm^2
Temperature	23.3 ± 0.8	°C
TiO$_2$ concentration	1 ± 0.05	mg/cm^2

Table 4
Health-related information of generated by-products.

Pollutant	REL (ppm)	REL data source	IARC carcinogenic classification
Formaldehyde	0.016	NIOSH	Group 1, carcinogenic to humans
Acetaldehyde	0.078	OEHHA[*]	Group 2B, possibly carcinogenic to humans
Acetone	250	NIOSH	–

* Office of Environmental Health Hazards Assessments, California Environmental Protection Agency, U.S.

where $C_{i,in}$ and $C_{i,out}$ are the upstream and downstream concentrations of by-product i in ppb, respectively.

To determine the risk level to human health associated with each photocatalytic system, a health-related index (HRI) was defined based on the concentrations of by-products and the recommended exposure limit (REL) values proposed by NIOSH (National Institute for Occupational Safety and Health, Table 4) [30].

$$HRI_{tot} = \sum \frac{C_{i,out}}{REL_i} \tag{3}$$

3. Results and discussion

3.1. Photocatalyst characterization

3.1.1. Crystal structure

Fig. 1a depicts the XRD patterns of TiO$_2$ prepared in neutral (pH~6) and alkaline solutions (pH = 10 and 12). The diffraction peaks at 25.3° and 30.8° respectively correspond to the anatase (101) plane (JCPDS No. 21-1272) and brookite (121) plane (JCPDS No. 29-1360). By increasing the pH of hydrothermal solution (i.e. increasing ammonia concentration), the brookite phase content steadily diminishes and ultimately at pH = 12 the brookite phase completely disappears. At higher pH values stronger and narrower diffractions peaks for anatase are obtained, implying the enhancement in crystallinity and substantial crystal growth. The average anatase crystal size (Table 5) for H-Base, H-A10, and H-A12 are 7.6, 10.7, and 18.8 nm, respectively, which is in good agreement with the peak sharpening seen in Fig. 1a. The improvement in crystallinity mainly stems from the fact that in a more basic reaction solution a larger population of hydroxyl groups are available for hydrolysis of titanium butoxide precursor.

Fig. 1b and 1c present the influence of acid type (sulfuric, nitric, acetic, formic, or hydrochloric) with pH = 2 and pH = 4, respectively, on phase structure. For all TiO$_2$ samples sharp peaks are seen at 25.3°, indicating formation of anatase crystals even at very low pH under hydrothermal conditions. Compared to other acids, HNO$_3$ more effectively catalyzes brookite phase formation (18.9% for H-NA2), which

was also witnessed in titania preparation via sol–gel [31] and hydrothermal methods [32]. The ability of acids to promote anatase formation followed the sequence of formic > sulfuric > acetic > nitric ~ chloric.

By comparing the values for relative crystallinity (Table 5), it is evident that basic hydrothermal solution leads to a significantly better crystallinity with respect to acidic or neutral solutions. In acidic solutions, due to the OH groups deficit, titanium precursor cannot be completely hydrolyzed and, therefore, a great quantity of unhydrolyzed alkyl groups exist in the reaction medium. These unhydrolyzed alkyl groups impede the coagulation and flocculation of titania particles (via electrostatic repulsion) and consequently the crystallization process [33].

Sulfuric acid and formic acid respectively result in the lowest (1.00–1.06) and highest (1.20–1.46) crystallinities among the investigated acids. It is possible that Cl$^-$, NO$_3^-$, or SO$_4^{2-}$ ions (or their complexes) remained in the precursors or crystal structure and caused disturbance in titanium dioxide crystallization. It is particularly noteworthy that none of the hydrothermal solutions provided the right conditions for rutile formation which could be explained from different standpoints. According to the Ostwald step rule, the titania phase with the lowest surface energy will first nucleates in the reaction medium. Since surface energy is inversely correlated to molar volume and anatase has a much higher molar volume with respect to rutile [16], anatase formation is preferred. The other justification is mainly related to the arrangements of octahedra in different phases of titania. In anatase, the TiO$_6$ octahedra are surrounded by eight octahedra: four edge-shared and four corner-shared, while in rutile, each octahedron is surrounded by ten octahedra: eight corner-shared and two edge-shared [34,35]. The edge-shared bonding between two octahedra requires two juxtaposed hydrolysis and condensation reactions while only one reaction is needed for corner-shared bonding. Considering this, at mildly acidic, neutral and basic conditions, due to the sufficient concentration of hydroxide ions, the probability of edge-shared bonding is larger; hence, anatase is the major phase observed in our experiments. Additionally, the formation of anatase at pH = 2 might be better explained by considering the status of TiO$_6$ octahedra in the reaction medium.
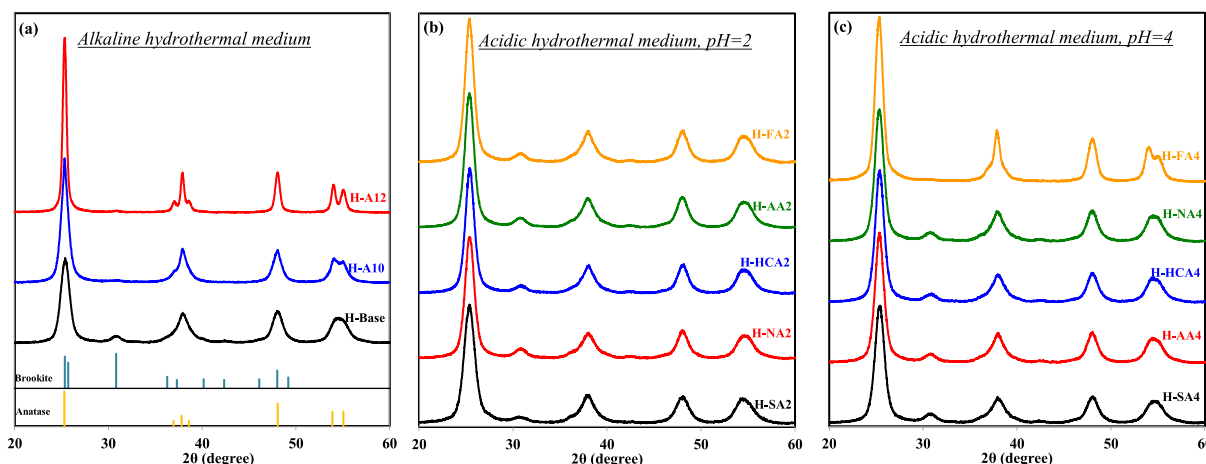

Fig. 1. XRD patterns of anatase and brookite TiO$_2$ (JCPDS database) and photocatalysts prepared under neutral/basic (a) and acidic environments (b).

Table 5
Properties of titania photocatalysts prepared at various hydrothermal conditions.

Sample	Relative crystallinity[a]	Phase content (%)		Crystal size (nm)		Surface area (m^2/g)	PL intensity[b]	PL intensity[c]
		Anatase	Brookite	Anatase	Brookite			
P25	4.17	81.3	18.7 (rutile)	25.8	27.4 (rutile)	52.0	–	–
H-Base	1.32	83.4	16.6	7.6	8.3	155.5	2177.5	258.1
H-SA2	1.00	88.7	11.3	6.7	7.5	216.1	893.7	257.7
H-SA4	1.06	86.1	13.9	8.3	7.9	179.8	3007.3	261.1
H-NA2	1.02	81.1	18.9	7.9	7.6	188.0	2162.0	272.4
H-NA4	1.20	83.7	16.3	8.1	8.0	173.0	2735.8	260.9
H-HCA2	1.05	85.2	14.8	7.5	7.6	180.5	2253.6	275.7
H-HCA4	1.19	82.7	17.3	8.2	7.9	161.0	2020.2	258.3
H-FA2	1.20	86.3	13.7	8.2	8.5	163.2	2100.0	270.5
H-FA4	1.46	100.0	0	9.2	–	151.2	2350.6	260.0
H-AA2	1.10	82.2	17.8	7.7	8.0	175.4	2385.4	269.7
H-AA4	1.17	84.3	15.7	8.2	8.0	171.9	2181.3	265.4
H-A10	1.90	97.8	2.2	10.7	–	121.0	2050.0	254.9
H-A12	2.65	100.0	0	17.5	–	82.9	3208.7	258.5

[a] Relative crystallinity is defined as the ratio between the intensity of (101) peak of each sample to that of H-SA2.
[b] PL intensity is the magnitude of fluorescence spectrum (presented in Fig. 5b) at ca. 425 nm.
[c] Fluorescence intensity is the magnitude of fluorescence spectrum (presented in Fig. 5a) at ca. 390 nm.

Under acidic environment, protonation of surface Ti‑OH groups [36] results in good dispersion of TiO$_6$ octahedra in the amorphous phase. These protonated surfaces (i.e. Ti‑OH$_2^+$) can combine with hydroxyl groups of other octahedra to form Ti‑O‑Ti bonds by dehydration (i.e. oxolation). It is suggested that this mechanism promotes face-sharing polycondensation and thus anatase formation [37,38]. It should be also mentioned that SO$_4^{2-}$ and CH$_3$COO$^-$ ions have strong affinity toward titanium atom in aqueous solution which hinders the structural rearrangement and phase transformation [16,39]. This gives anatase formation a kinetic advantage over rutile in terms of lower activation energy for crystallization. Regarding the formation of brookite in the acidic and neutral solutions, it is to be noted that the activation energy for anatase → brookite transformation is smaller (11.9 kJ/mol) than that of brookite → rutile (163.8 kJ/mol) [40], consequently under low hydrothermal temperature of 180 °C, the former process prevails. On the other hand, Yu et al. [41] put forward an explanation for the formation of brookite phase in the acidic environment containing chloride ions. Considering the fact that the ligand field strength of chloride ion is greater than that of the butoxy group, Cl can replace the butoxy group (i.e. OC$_2$H$_9$) in Ti(OH)$_x$(OC$_2$H$_9$)$_x$ complex formed during hydrolysis. In the aqueous solution, Ti(OH)$_2$(Cl)$_2$ exists in the form of Ti(OH)$_2$Cl$_2$(H$_2$O)$_2$, which is believed to be the precursor of brookite [42].

3.1.2. Surface area and porosity

Nitrogen sorption analysis can be used to gain insights into the catalyst pore texture and specific surface area. Figs. 2a and 2b exhibit the N$_2$ adsorption-desorption isotherms and the pore size distributions of H-Base, H-A12, and H-SA2, respectively. As can be seen in Fig. 2a, H-Base and H-SA2 both indicate isotherms of type IV (BDDT classification) with the hysteresis loops around $0.50 < p_0/p < 0.85$. The type IV isotherms suggest that the porosity in these samples is mainly due to the existence of mesopores. The hysteresis loops of H-Base and H-SA2 have a triangular shape with steep desorption branch which can be categorized as type H2 hysteresis loop, associated with narrow necks and wider bodies (ink-bottle pores). Additionally, the isotherm of H-SA2 also shows a very small H3 type hysteresis loop at $0.9 < p_0/p < 1.0$, suggesting a bimodal pore size distribution in the mesoporous region. The isotherm of H-A12 is of type II unlike the other samples and the hysteresis loop appears at higher relative pressure, $0.70 < p_0/p < 1.0$, indicating formation of larger mesopores. The steep increment in the adsorption branch (seen in H-A12) is attributed to the capillary condensation of N$_2$ within titania mesopores (2–50 nm). Moreover, the shape of H-A12 hysteresis loop is of type H3, which could be observed in slit-like pores result from aggregation of plate-like particles. With increasing the pH of the reaction medium, the hysteresis loop shifts rightward and downward to the region with smaller adsorbed N$_2$ volume and higher relative pressure. This implies that in a more basic environment photocatalyst with larger pores and smaller specific surface area can be obtained. The increment in catalyst pore size with pH could also be noticed in the pore size distributions presented in Fig. 2b.
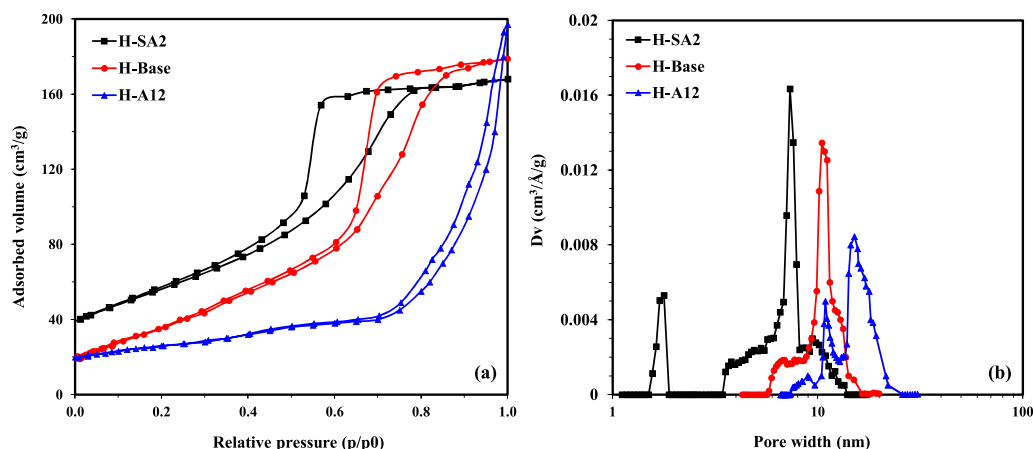

Fig. 2. Nitrogen adsorption–desorption isotherms and pore-size distribution of H-Base, H-SA2, and H-A12.
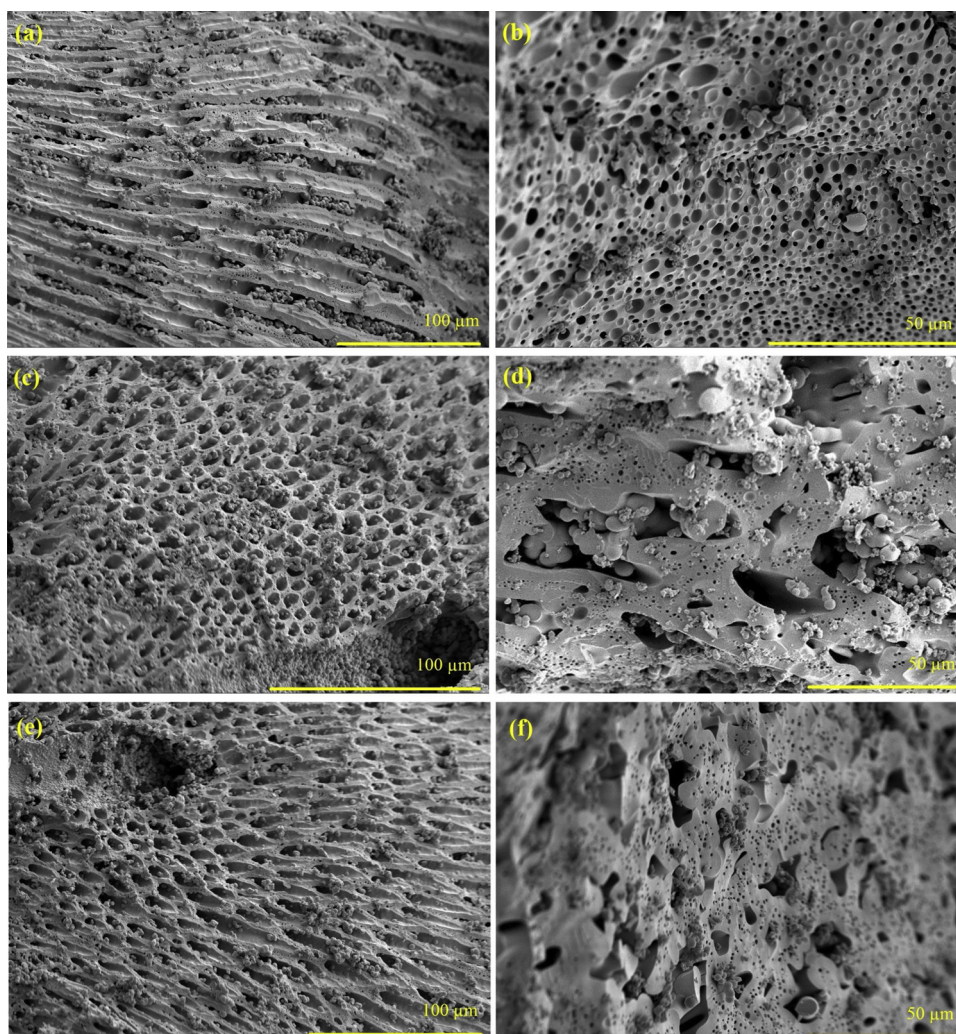
Fig. 3. SEM images of (a, b) H-Base, (c, d) H-SA2, and (e, f) H-A12.

The photocatalyst prepared at pH = 2 shows a relatively narrow pore size distribution mainly between 3.4 and 14 nm, centered at 7.3 nm. For higher pH values, the pore size distributions become wider and center at larger pore sizes: 10.5 nm for H-Base and 15.1 nm for H-A12. This can be mainly attributed to the enlargement of anatase crystals in more alkaline conditions which upon aggregation form larger mesopores. The BET surface areas of TiO_2 photocatalysts prepared at different hydrothermal media are listed in Table 5. It can be noticed that the hydrothermally-synthesized samples have much larger surface areas (82.9-216.1 m^2/g) compared to commercial P25 (52.0 m^2/g). On the other hand, in general, the surface area substantially diminishes as the pH value of hydrothermal solution increases. For instance, the surface areas of titania samples prepared in pure water (H-Base) and concentrated ammonia (H-A12) are respectively 28% and 61% smaller than H-SA2. At each acidic pH level (i.e. 2 or 4), comparable specific surface areas are seen for different acids.

3.1.3. Morphological structure

The porous structure of TiO_2 photocatalysts in the micrometer range was studied by scanning electron microscopy. Fig. 3 demonstrates the SEM images of H-SA2, H-Base, and H-A12 at two different magnifications, in which the macroporous structure of catalysts can be easily seen. Basically, three forms of porosity can be noticed: (i) long and well-oriented macrochannels that are parallel to each other and perpendicular to the outer surface of the particle, (ii) surface macropores of 0.8–9.3 μm in size, and (iii) porous walls with pores mostly smaller than

0.5 μm. Considering the fact that no surfactant or template was used in the preparation process, the macropores sizes differ and a certain degree of randomness can be seen in the structure of the samples. In the course of titanium precursor hydrolysis and subsequent condensation reactions, butanol was released into the aqueous solution, which could create microphase-separated regions of solid Ti particles and water-alcohol channels. This can provide the right condition for the formation of macrochannels which are observed in the SEM images. The hydrothermal route could successfully advance titanium dioxide crystallization while maintaining the hierarchically porous network initially formed during hydrolysis and aging processes. It is noteworthy that these open-ended tubelike macrochannels can facilitate the diffusion of VOC molecules to the active sites of titania and also serve as paths for emitted photons to reach particle's interior regions. Nonetheless, as illustrated in Fig. 3, in some regions, titania particles could not incorporate into the main porous structure and fused together in the form of dimers or trimmers which may block the macropores (more details in Supplementary Material). Using energy dispersive spectroscopy (EDS), it was showed that these agglomerated particles are also pure TiO_2 (Fig. S2 and Table S2).

TEM was employed to further elucidate the microstructure of hydrothermally-prepared TiO_2 photocatalysts. Fig. 4 presents the TEM and HR-TEM images of H-Base, H-SA2, and H-A12. No long-range ordered mesoporous structure can be seen in Fig. 4a, b, or c, which indicates that a major portion of mesopores are originated from the aggregation of small titania crystals (i.e. interparticle porosity). In good
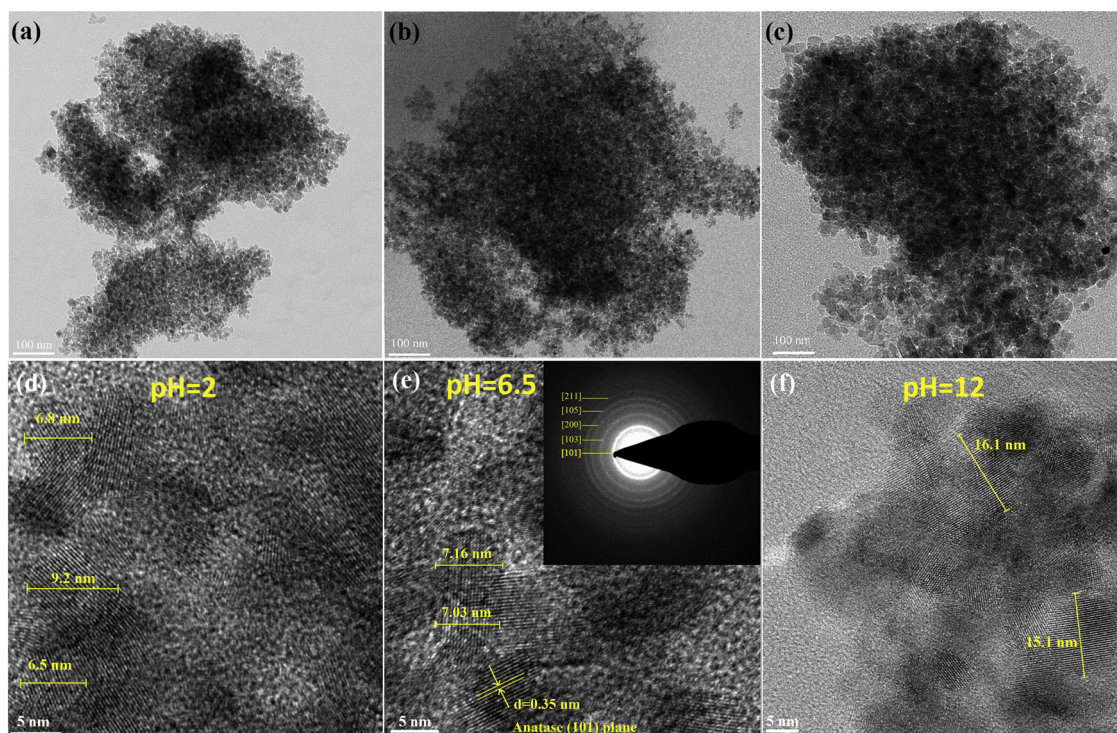
Fig. 4. (a, b, c) TEM and (d, e, f) HR-TEM images. Inset of 4e: SAED pattern of H-Base. (a, d) H-SA2, (b, e) H-Base and (c, f) H-A12.

accordance with the BET results, depending on the sample, mesopores ranging from ca. 2 nm to ca. 30 nm in size are formed due to the accumulation of TiO_2 nanocrystals. As the pH of reaction medium is raised from 2 to 12 (i.e. H-SA2 to H-A12), the interparticle pore size grows as well. The HR-TEM images reveal that the crystallinity and crystal size are improved in more alkaline preparation environments. Anatase crystal sizes measured directly from HR-TEM images (Fig. 4d, e, and f) are about 7, 6.5, and 15.5 nm for H-Base, H-SA2, and H-A12, respectively. The clarity of lattice fringes of titania crystals in HR-TEM images, specifically in Fig. 4f, suggests high degree of crystallinity for all samples. The lattice fringes are around 3.5 Å, corresponding to the (101) plane of anatase [43]. The polycrystalline anatase phase is, demonstrated by SAED pattern (inset in Fig.4e), complying with the results of the XRD analysis. Clear diffraction rings indexable to anatase (*d*-spacings and (*hkl*) values: 0.352 (101), 0.243 (103), 0.189 (200), 0.169 (105), and 0.166 nm (211); JCPDS no. 21-1272) further shows that H-Base has good crystallinity. It is worth mentioning that the particle size distributions of yielded titania samples (not shown) were fairly narrow. Producing uniformly sized or monodispersed particles is in fact one of the known advantages of hydrothermal route. The reason is that in the hydrothermal route, crystallization and crystal growth occur in a homogeneous condition, therefore, the crystal size distribution is fairly narrow.

3.1.4. Photoluminescence and hydroxyl radical analyses

Photoluminescence spectroscopy can be employed to investigate the efficiency of charge carriers generation and separation. Considering the fact that electron-hole recombination in titanium dioxide results in PL emission, PL analysis provides valuable information on the availability of electrons and holes for photocatalytic reactions [44]. The PL spectra of photocatalysts prepared in various hydrothermal reaction media are illustrated in Fig. 5a. To facilitate the comparison between different spectra, only some samples are represented in Fig. 5a and instead all PL intensities (at 390 nm) are listed in Table 5. In the wavelength range of 330-570 nm, the shapes of spectra are very similar and only small shifts can be noticed for the main emission peaks. Deconvolution of H-SA2 spectrum is presented in the inset of Fig. 5a, which indicates that the

spectra consist of one strong peak at about 390 and four weaker peaks at 424, 445.5, 489, and 532 nm. The strong peak at about 390 nm (depending on the catalyst) is due to the emission of band gap transition, with the energy of light close to the band gap energy of anatase (387.5 nm) [45]. The emission peak appears at 424 nm can be attributed to the indirect band edge allowed transitions and self-trapped excitations localized in TiO_6 octahedra [46,47]. The latter is the result of interaction between conduction band electrons (on Ti 3d orbital) and holes in the O 2p orbital of TiO_2 [44]. The emission bands at 445.5 and 489 nm can be assigned to excitonic PL, which mainly originate from surface oxygen vacancies, crystal defects, and/or self-trapped excitations in TiO_6 [48,49]. It is noteworthy that oxygen vacancy is an intrinsic defect in TiO_2 lattice which traps the e^-/h^+ and creates the intermediate energy states in the forbidden gap. There is also a PL band at 532 nm, which can be attributed to the oxygen vacancies, impurities and defects [50,51]. PL intensities of photocatalysts (reported in Fig. 5a and Table 5) reveal that the emission intensity to some extent agrees with photocatalyst crystallinity. In this regard, H-HCA2 which has one of the lowest crystallinities among prepared samples exhibits the highest PL intensity, suggesting significant charge carriers recombination. On the other hand, H-A10 and H-Base, which comparatively possess higher crystallinities, show weaker PL emissions. Enhancement in photocatalyst crystallinity reduces the number of crystal defects that potentially instigate the recombination of electrons and holes. Nonetheless, it is noteworthy that a number of anomalies were recognized in the PL spectra of our samples (see Table 5), where photocatalysts with low crystallinity exhibited low PL intensity (e.g. H-SA2).

Photocatalyst's charge separation efficiency directly influences the photochemical reactions that lead to the formation of •OHs, the main oxidants of VOCs during photocatalytic air purification. Fluorescence spectrometry technique with terephthalic acid (TA) as probe molecule was used to compare the ability of titania samples to produce •OH. Hydroxyl radicals quickly react with TA and produce highly fluorescent 2-hydroxyterephthalic acid (2-HTA); thus, intensity of the PL peak of 2-HTA is proportional to the population of •OH on the surface of photocatalyst. The PL spectra of TiO_2 photocatalysts prepared at different hydrothermal conditions are demonstrated in Fig. 5b. The inset of
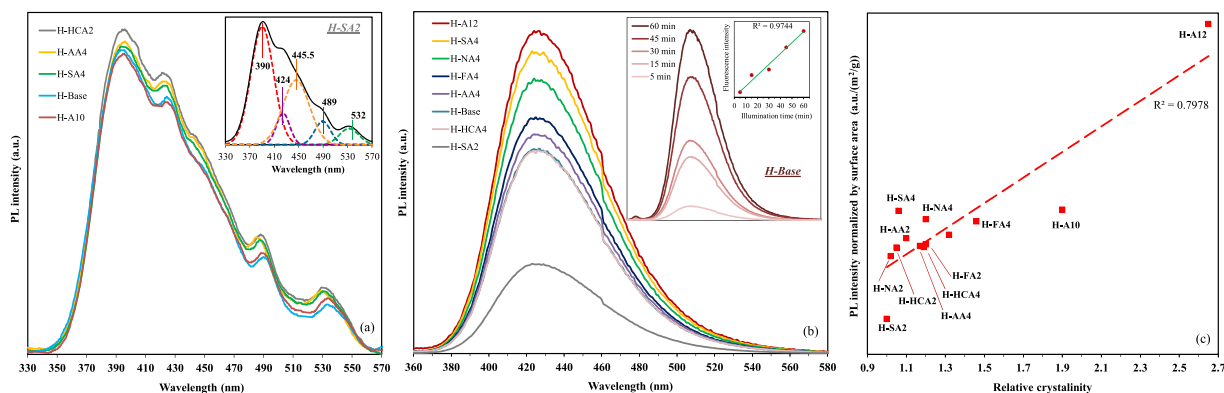
Fig. 5. (a) Photoluminescence spectra, inset: deconvolution of H-SA2 spectrum. (b) Fluorescence spectra, inset: variation in PL intensity of H-Base irradiated for various durations. (c) Dependence of PL intensity on photocatalyst crystallinity.

Fig. 5b depicts the fluorescence spectra that are obtained from supernatant liquid of H-Base titania irradiated for different durations (from 5 to 60 min). The linearity of PL intensity with time suggests that the number of generated ˙OHs is proportional to irradiation time. For the sake of clarity, only sufficiently distinct PL spectra are depicted in Fig. 5b and the maximum PL intensities at 425 nm for all samples are listed in Table 5. H-SA2 has a relatively small PL intensity, which is obviously related to its low crystallinity. By increasing the pH value of the reaction medium to 4, an increment in the PL intensity is seen for all acids except hydrochloric acid (Table 5), which surprisingly shows a small diminution in PL intensity for H-HCA4. The enhancement in crystallinity results in fewer recombinations, more e^{-}-h^{+} pairs, and higher concentrations of ˙OH (i.e. 2-HTA) which could explain the stronger PL emissions. Despite the fact that the relative crystallinity of H-HCA4 is greater than H-HCA2 (1.19 vs. 1.05), H-HCA2 has slightly larger PL intensity compared to H-HCA4 (2253.6 vs. 2020.2 a.u.). This could be rationalized by comparing the key properties of H-HCA2 and H-HCA4: (i) H-HCA4 has a larger brookite content (17.3 vs 14.8%) and (ii) H-HCA4 specific surface area is roughly 11% smaller than H-HCA2, both (i) and (ii) contributing to lower PL intensity. By employing an alkaline hydrothermal solution (i.e. H-A12) an increase in the PL intensity can be noted which could be anticipated given the huge gap between the relative crystallinity of H-A12 and other samples.

Fig. 5c demonstrates the variations in PL intensity (obtained from fluorescence spectroscopy) with relative crystallinity of photocatalysts. The surface area normalized PL intensity (calculated based on the data in Table 5, using surface area and PL intensity) and relative crystallinity exhibit an acceptable level of proportionality (red trend line, $R^2 = 0.79$). The positive correlation suggests that a greater number of ˙OHs can be produced on the surface of titania samples with better crystallinity. On the basis of this trend, it can be concluded that once the contribution of surface area is excluded, among various features of catalyst (e.g. crystallinity, anatase content, crystal size, and band gap), the governing factor in generation of hydroxyls radicals on TiO_2 is crystallinity.

3.1.5. XPS and IR studies

XPS is considered a reliable method to acquire information regarding the chemical states and surface chemical compositions of photocatalysts. The XPS survey spectra of H-SA2, H-A12, and H-Base are presented in Fig. 6a, indicating that all three titania samples contain Ti, O, and C elements. Besides small quantities of carbon and sulfur (only for H-SA2), no other impurities were observed in the XPS surveys. The C1 s peak located at a binding energy of approximately 285 eV is assigned to adventitious carbon. Fig. 6b shows high-resolution XPS spectra of O1 s region after Gaussian curve fitting, revealing presence of different types of oxygen on photocatalyst surface. The O1 s can be mainly fitted into two peaks: a main peak at 530.3 eV and a smaller one

at 531.8 eV which are respectively ascribed to lattice oxygen (Ti –O) in TiO_2 crystals and surface hydroxyl group (Ti–OH) [15,52]. The peak area of hydroxyl groups of H-SA2 sample is much larger than those of H-Base and H-A12, indicating that the former contains more hydroxyl groups. As reported in Table 6, the OH/O_{tot} ratio for photocatalysts declines with increasing the pH of hydrothermal reaction medium. This is due to the fact that at a higher pH, hydrothermal reactions further proceed; thus, many surface hydroxyl groups are consumed in condensation reactions to form Ti-O-Ti networks. Additionally, the stronger OH peak for H-SA2 can also be partly attributed to its larger surface area compared to the other two samples. Fig. 6c illustrates the high resolution XPS spectra of C1s region of photocatalysts. The C 1s region can be deconvoluted for three peaks at bindings energy of 284.7, 286.2, and 288.7 eV. The main peak (at 284.7 eV) represents carbons in saturated hydrocarbon groups (C−C and C−H) [53] which could result from residual carbon in the hydrothermally-prepared samples or the adventitious carbon. The small peaks at 286.3 and 288.7 eV, respectively correspond to hydroxyl carbon (C−OH) and carboxyl carbon (C═O) [54–56]. Regarding the Ti 2p spectra (Fig. 6d), the peaks at 464.8 and 458.6 eV are attributed to Ti^{4+} 2p 1/2 and Ti^{4+} 2p 3/2, respectively, showing the oxidation state of the Ti element is the same as the bulk TiO_2. In addition, the small peak located at 457.9 eV which was evidenced only for H-SA2 is attributed to Ti^{3+} 2p 3/2. The peak at 457.9 eV signifies that there are a small number of oxygen vacancies on the surface of H-SA2 [57].

The atomic ratios of Ti to O of all samples are in good agreement with the nominal atomic composition of TiO_2 (Table 6). The carbon can be attributed to the residual carbon from the sample and adventitious hydrocarbon from XPS instrument itself. Excessive O element could come from the chemisorption of water on the samples [58].

To further investigate the surface chemistry of developed photocatalysts FTIR analysis was employed. The FTIR spectra of H-SA2, H-A12, and H-Base are presented in Fig. 7 over the OH spectral region. The intense absorbance around $1640 \, cm^{-1}$ is ascribed to the bending mode of adsorbed water. A broad and strong absorption band appears for all samples in the 3600-2800 cm^{-1} range. This peak is generally attributed to OH groups, H_2O molecules adsorbed on Ti^{4+} cation and undissociated water molecules attached to the surface by hydrogen bonds [59,60]. As can be seen in Fig. 7, H-SA2 possesses stronger absorption bands in the 3600-2800 cm^{-1} range and $1640 \, cm^{-1}$ with respect to H-Base and H-A12. As already discussed, titania samples prepared at higher pH values have smaller surface areas, which means H-Base and H-A12 contain lower amounts of adsorbed water. On the other hand, since in a highly alkaline environment condensation reactions are promoted, a part of surface hydroxyl groups are utilized during Ti-O-Ti formation. FTIR spectrum of H-SA2 also shows two weak bands at 2854 and 2924 cm^{-1}, which can be due to C−H stretching vibration. These bands could originate from the unhydrolyzed butoxy groups (or other
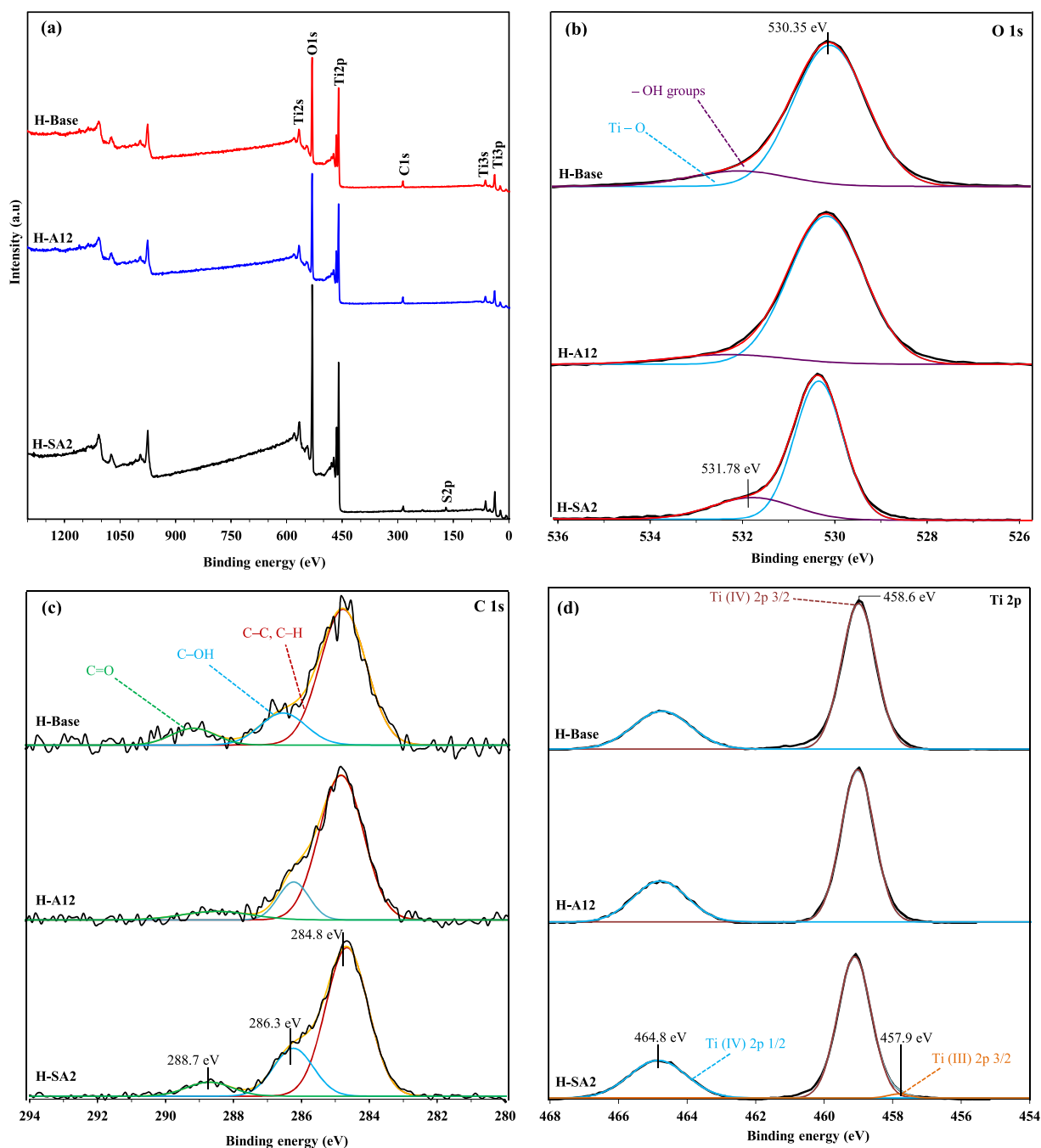
Fig. 6. (a) XPS survey spectra of H-Base, H-SA2, and H-A12. (b, c, and d) High resolution XPS spectra of O1s, C 1s, and Ti 2p regions.

Table 6
Elemental surface composition (atomic %) and ratio of hydroxyl groups oxygen to lattice oxygen.

Photocatalyst	Element				OH/O_{tot}
	Ti	O	C	S	
H-Base	25.8	64.6	9.6	–	0.15
H-A12	26.5	63.0	10.5	–	0.09
H-SA2	25.4	64.4	7.5	2.7	0.25

residual organic moieties) in H-SA2 sample, confirming the results of XPS (Fig. 6c). Several peaks at frequencies higher than 3600 cm^{-1} are seen in the spectra of all three samples at 3634, 3675, 3695, 3716, and 3732 cm^{-1}. These bands are generally assigned to the bridged − OH (Ti − OH − Ti) and terminal hydroxyl groups (Ti − OH) [49,52,55]. As can be easily noticed in the magnified figure of 3600-3750 cm^{-1} region, compared to H-SA2 and H-A12, H-Base has stronger bands at 3634 and 3695 cm^{-1}, indicating larger population of isolated hydroxyl groups [61].

3.2. Photocatalytic activity

The overall performance of a photocatalyst strongly depends on a number of factors including crystallinity, crystal size, surface area, porosity, crystalline phase, charge-separation efficiency, light harvesting ability, surface chemistry, and the ability to produce ˙OHs. Besides, the magnitude of influence of each factor on the performance of photocatalyst is closely linked to the key operating conditions such as relative humidity, inlet concentration, airflow rate and light intensity.
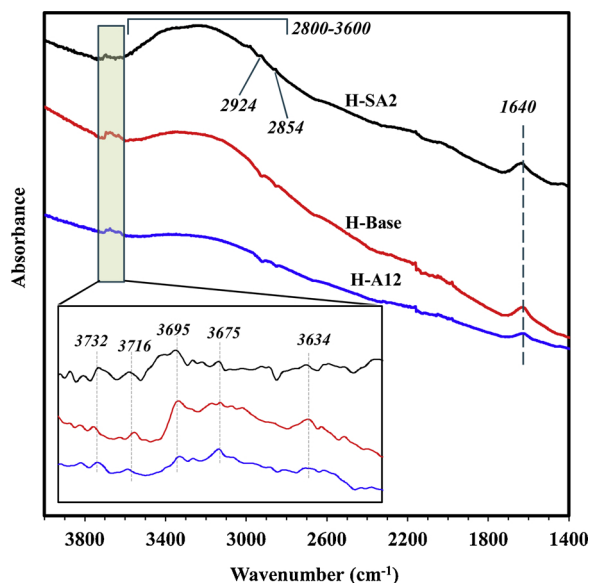
Fig. 7. FTIR spectra of H-Base, H-SA2, and H-A12 in OH spectral range.

Accordingly, it is of great practical use to evaluate the activity of developed TiO_2 photocatalysts under realistic conditions. In the present study, the photocatalytic activity of hierarchically porous titanium dioxides were assessed at wide ranges of residence time (i.e. airflow rate), relative humidity, and MEK inlet concentration to pinpoint the governing characteristics of a photocatalyst for air purification.

3.2.1. Impact of airflow rate

Airflow rate directly determines the contact time between the pollutants and the photocatalytic air filter. In this study, residence time is defined as the ratio of the thickness of nickel foam filter to the face velocity. Fig. 8 demonstrates the variation in removal efficiency of various photocatalysts with residence time in the range of 0.012-0.03 s. Expectedly, for all photocatalysts higher values of removal efficiency are reached at longer residence times since MEK molecules have more

time to penetrate the boundary layer, adsorb on the surface, and react with the active species (e.g. hydroxyl radicals). However, it is interesting to note that the extent of the influence of residence time on the performance is closely related to the characteristics of photocatalyst, specifically surface area. As can be seen in Fig. 8, depending on the residence time, the maximum removal efficiency of MEK is achieved over different titania photocatalysts: H-NA4 at 0.012 s (36.9%), and H-A10 at 0.02 s (48.0%) and 0.03 s (61.4%). This is understandable considering the fact that at shorter residence times the role of surface area (and porosity) in the overall VOC removal is more dominant with respect to that of crystallinity. In other words, for a catalyst with small surface area (e.g. H-A10), the short residence time severely limits the mass transfer of pollutants from the bulk to the surface and adjacent to the active sites/species [62]. As a result, in the case of H-A10, even though the high degree of crystallinity can guarantee a large density of OH radicals on the surface (as evidence in Fig. 5b and Table 5), the inefficient adsorption does not bring MEK molecules into contact with $^{\cdot}$OHs and, thus, impairs the removal efficiency [63]. In contrast, at a longer residence time (i.e. 0.02 or 0.03 s), more MEK molecules are available on the surface of H-A10 and the oxidation reactions will be the determining step. To better understand this point it could be helpful to compare the relative performance drops (defined as: $1 - \frac{\eta_{t=0.012\,s}}{\eta_{t=0.03\,s}}$) of H-NA4 and H-A10. The relative performance drops for H-NA4 and H-A10 are 0.33 and 0.42, respectively, which clearly points to the fact that H-A10 is more sensitive to the changes in airflow rate. Except H-A12, all other hydrothermally synthesized TiO_2 samples significantly outperform P25 in MEK removal efficiency primarily due to the large surface area, multiscale porous structure, and sufficiently high crystallinity.

Fig. 9 presents the corresponding by-products generation for the hydrothermally-prepared catalysts and P25. In the outlet air stream formaldehyde, acetaldehyde, acetone and traces of propionaldehyde were detected as unwanted by-products along with CO_2 as the main product. As a general trend, the total amount of by-products grows with the residence time clearly due to the increment in degradation rate. At longer residence times, more MEK molecules can adsorb on the surface and participate in the catalytic reactions, leading to formation of larger amounts of intermediates/by-products [1,62]. However, since
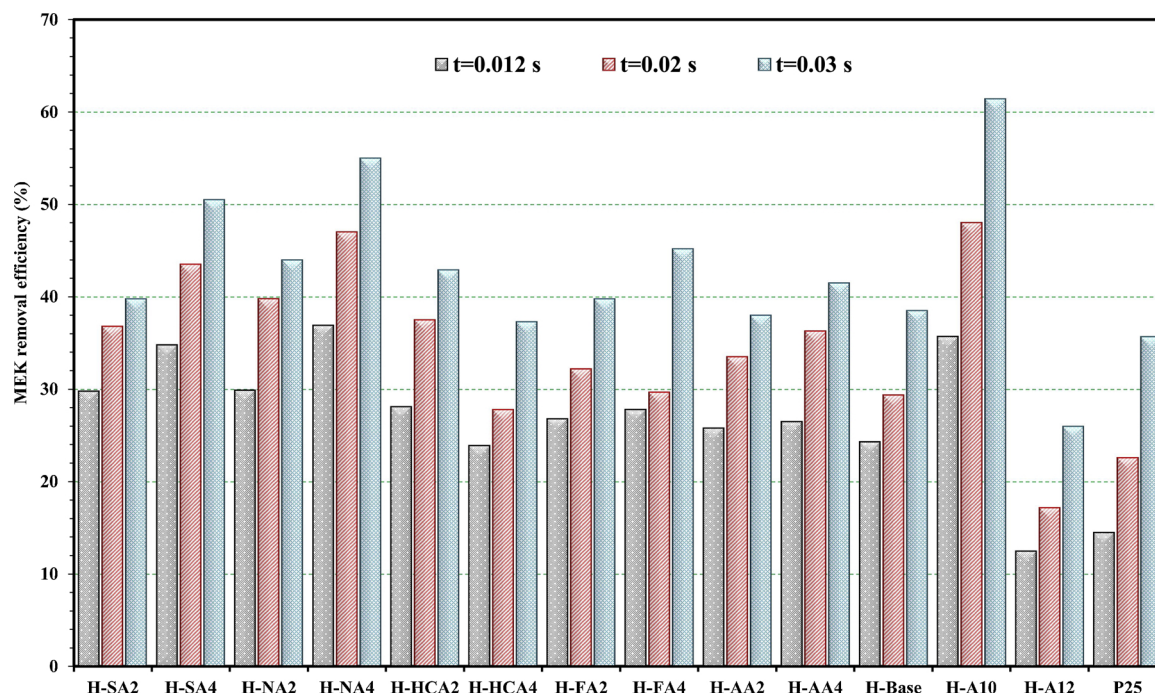

Fig. 8. Effect of residence time on MEK removal efficiency over various photocatalysts. [$C_{MEK,\ in}$] = 1 ppm, relative humidity = 50%, light intensity = 50 W/m^2.
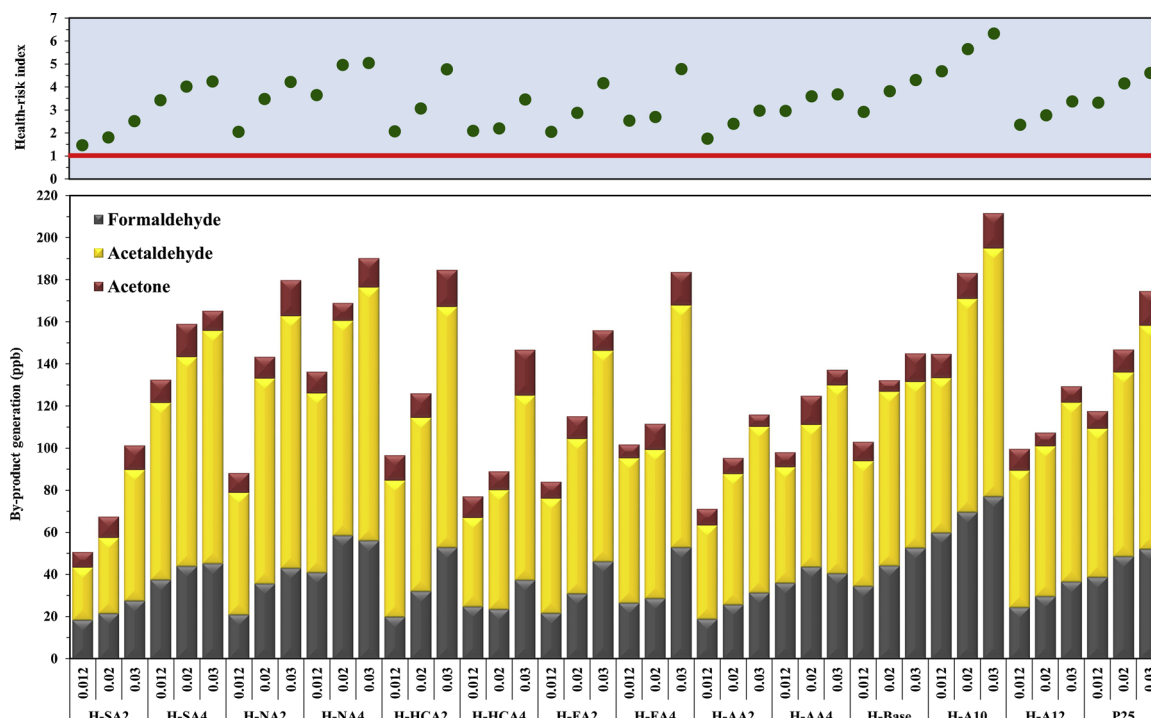
Fig. 9. Effect of residence time on by-products generation during MEK photocatalytic degradation. [$C_{MEK,\ in}$] = 1 ppm, relative humidity = 50%, light intensity = 50 W/m^2.

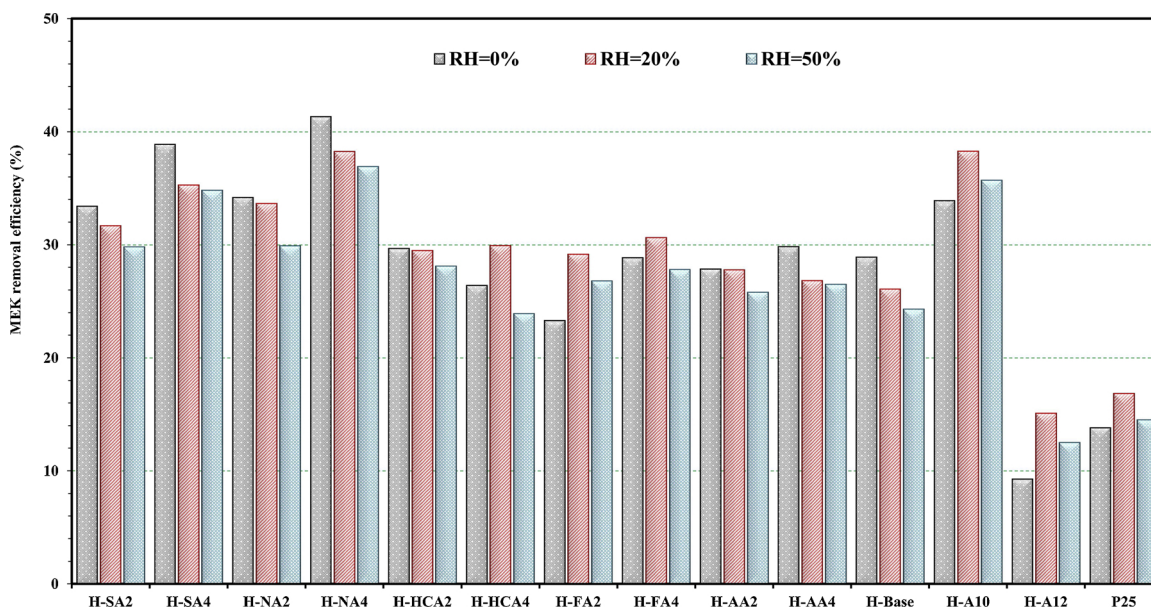**Fig. 10.** Effect of relative humidity on MEK removal efficiency over various photocatalysts. [$C_{MEK,\ in}$] = 1 ppm, residence time = 0.012 s, light intensity = 50 W/m^2.

intermediates/by-products as well have a higher chance of reaction and re-adsorption on the surface as the airflow rate decreases, the increase in the amount of by-products does not exactly correspond with the enhancement in the efficiency. For instance, MEK removal efficiency enhances from 35.7% at t_{res} = 0.012 s to 61.4% at t_{res} = 0.03 s, while the total amount of by-products increased from 144.7 ppb to only 211.5 ppb. On the other hand, it can be noticed that in the majority of cases and especially at t_{res} = 0.012 s, despite the fact that the removal efficiency is much higher on the high-surface-area and hierarchically porous samples than on P25, the amounts of by-products are comparatively lower. The reason is that the multimodal porous TiO$_2$ with an interconnected structure more efficiently traps the intermediates,

barricades their release to the gas phase, and advances total mineralization [13]. Generation of unwanted by-products is one of the main shortcomings of photocatalytic air purification. It has been demonstrated that under severe operating conditions, the treated air may exert even more health risks to human because it carries by-products which are more harmful than the original contaminant [64]. Consequently, in the present study we analyze this issue by assessing the health-risk index for generated by-products during PCO of MEK under various operating conditions. The top graph in Fig. 9 displays the variation in HRI (eq. 3) with the residence time over different photocatalysts. As could be expected from the trends of by-products generation, the higher the residence time is, the larger the HRI is. The HRI value varies

between 1.47 and 6.32, which is reasonable considering that the inlet concentration of MEK is 1000 ppb. Among the generated by-products, formaldehyde is the most hazardous one with a REL value of 16 ppb and known to be a carcinogen. Consequently, the amount of formaldehyde in the outlet stream most severely affects the HRI value.

3.2.2. Impact of relative humidity

Presence of high concentrations of water vapor (up to 22,000 ppm) in air especially during summer is a serious yet inevitable barrier against efficient removal of pollutants. In this study, the impact of relative humidity on the efficacy of developed titania samples is investigated by performing the PCO tests at three humidity levels: 0, 20, and 50%. As can be seen in Fig. 10, the response of photocatalyst to the increment in relative humidity (from 0 to 50%) follows one of two trends: (i) steady reduction in MEK removal efficiency or (ii) presence of an optimum performance at 20% relative humidity. The first trend can chiefly be attributed to the adsorption competition between water and MEK molecules over the active sites of titania [65]. In addition, the strong hydrogen bonds between water molecules and surface hydroxyl groups result in the formation of a water film on TiO$_2$. The water film diminishes the attraction forces between MEK molecules and titania and exacerbates the adsorption process [66]. This adverse effect is less noticeable for photocatalysts with large surface area (e.g. H-SA2, H-NA2, etc) since these samples are more capable of hosting both MEK and water molecules. For instance, MEK removal efficiency over H-SA2, H-NA2, and H-HCA2 only drop by 3.6, 4.3, and 1.6% respectively as humidity increases from 0 to 50%. It is important to note that the hydrophilic character and high water solubility (i.e. polar) of MEK enable it to diffuse through or adsorb on the water film which lessen the influence of humidity on the adsorption process [67]. In the second trend, which is mostly observed for photocatalysts with small porosity and surface area, MEK removal efficiency firstly improves with humidity, peaks at humidity of 20%, and afterwards decreases. To explain this behavior one should keep in mind that besides surface hydroxyls, water vapor is the major source of ·OHs. Water molecules on the surface of titania react with holes and produce ·OHs, the main oxidant during MEK degradation. Therefore, it is logical to presume that for low surface area (i.e. highly crystalline) TiO$_2$ catalysts which also have low OH density (Figs. 6b and 7), at dry condition, the precursor for ·OH formation is missing, leading to a substantial performance drop. As an example, when humidity increases from 0 to 20%, MEK removal efficiency over H-A12 grows by roughly 63% compared to its initial value simply because more ·OHs are available for oxidation of MEK. Further increment in relative humidity (i.e. 50%) deteriorates the efficiency since the inhibiting effect of adsorption competition overpowers the promoting effect of ·OH formation.

Humidity level can also influence the amount and type of generated by-products as depicted in Fig. 11. In general, the amount of by-products increases with relative humidity because the adsorption competition between the intermediates/by-products and water molecules for active sites of titania becomes more severe. Nevertheless, it should be highlighted that the abundance of hydroxyl radicals at higher humidity levels can boost the total mineralization and reduce the by-products. As a result, in some cases (e.g. H-SA2, H-FA4, and H-A12) the amount of by-products at 50% is equal or even lower than that at 20%. Compared to the residence time (Fig. 9), HRI is less sensitive to the changes in relative humidity and mainly fluctuates between 1 and 3. H-SA2 offers the safest PCO system (HRI = 1.41–1.52) since its superior surface area, OH population, and adsorption capacity prevent the desorption of by-products from the surface to the air.

3.2.3. Impact of pollutant inlet concentration

The influence of MEK inlet concentration on removal efficiency over various TiO$_2$ samples is illustrated in Fig. 12. In line with previous studies, raising the pollutant concentration leads to a sharp decline in removal efficiency (between 8–22.9%) in all cases. This is understandable considering that the ratio of the number of "active/adsorptive sites + reactive species" to that of incoming MEK molecules decreases as the concentration increases [68]. As a consequence, a greater number of MEK molecules cannot participate in the degradation reactions with ·OHs. It is noteworthy that in indoor environment (i.e. office, residential, and commercial buildings) although there are numerous pollutants, the concentration of each VOC normally does not go beyond 20 ppb. Therefore, the values of removal efficiency at [C$_{MEK}$] = 100 ppb are better representatives of the actual performance of the developed photocatalysts. By raising the hydrothermal medium pH from 2 to 4, MEK removal efficiency improves for all samples except with hydrochloric acid. At [C$_{MEK}$] = 100 ppb, H-SA4, H-NA4, H-FA4, and H-AA4 outperform their counterparts prepared at pH = 2 by 6.2, 11.9, 3.7 and 1.5% respectively. The observed behavior can be mainly attributed to the improvement in crystallinity of titania samples at higher pH values which results in higher quantum efficiency and lower recombination of e$^-$-h$^+$ pairs. This indicates that for these samples the improvement in crystallinity outweighs the decline in surface area and porosity; therefore, the net effect of increasing solution pH is positive. On the other hand, the upward trend in MEK removal efficiency with pH corresponds well with the ability of these photocatalysts to create ·OHs. As can be seen in Table 5, for sulfuric, nitric, and formic acids, PL intensity is greater for the catalyst prepared at pH of 4, which implies larger concentration of hydroxyl radicals. Interestingly, for hydrochloric acid, both MEK removal efficiency and PL intensity experience downward trends by increasing the aqueous solution pH. Porosity and surface area diminution, and the increase in brookite phase content might be considered as the main reasons for the efficiency (and PL intensity) drop from H-HCA2 to H-HCA4. H-SA2 has the lowest crystallinity among the samples which leads to an extremely low PL intensity (893.7 a.u.); nevertheless, it reaches a comparable MEK removal efficiency. A certain contributing factor is H-SA2 surface area (and porosity) which exceeds all other samples prepared in acidic environments by 13–30% and provides H-SA2 a great advantage in the adsorption step. The photocatalyst prepared in ammonia alkaline solution with pH of 10 achieves the highest MEK removal efficiency, 61.4%, which is 26% higher than that of P25. The relative crystallinity and surface area of H-A10 are 1.9 and 121 m^2/g respectively, which apparently offer the best trade-off between these two contradictory features. In photocatalysis, charge carriers must reach and be stabilized at the surface of titania for e-/h$^+$ transfer processes [33]. These phenomena are extremely hampered by recombination of e–h$^+$ pairs in bulk and on the surface of photocatalyst. Bulk and surface recombinations exacerbate with increment and decrement in crystal size, respectively. Consequently, it is logical to presume that at a specific crystal size the optimum balance between bulk and surface recombinations can be reached. Fluorescence spectrometry (OH radical generation) and photoluminescence results support the superior performance of H-A10. As can be seen in Fig. 5c, H-A10 has the second highest surface area normalized PL intensity (16.94 a.u./(m^2/g)), indicating the presence of a large number of hydroxyl radicals on the surface owed to satisfactory e–h$^+$ separation. On the other hand, the weak PL emission for H-A10 (Table 5) also confirms the long lifetime of charge carriers on H-A10. It was witnessed that further increment in the hydrothermal solution pH (i.e. from 10 to 12) entails a drastic fall in MEK removal efficiency to 26%. As shown in Table 5 and Fig. 5b, H-A12 has the highest degree of crystallinity and PL intensity which are advantageous to PCO processes. However, the low surface area, decline in mesoporosity (Fig. 2), small population of surface hydroxyl groups (Figs. 6 and 7), and excessive crystal growth could be held accountable for the inferior activity of H-A12. It is worth noting that in our experiments photocatalysts with 100% anatase phase (i.e. H-A12 and H-
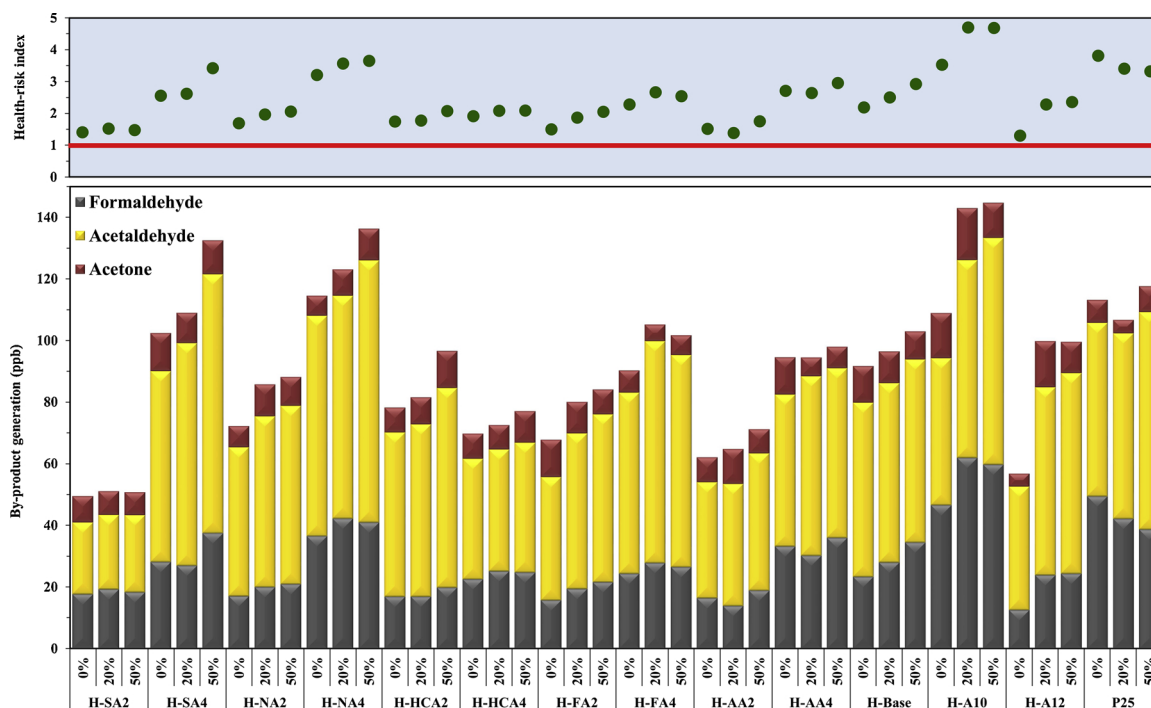
Fig. 11. Effect of relative humidity on by-products generation during MEK photocatalytic degradation. $[C_{MEK,\ in}] = 1$ ppm, residence time = 0.012 s, light intensity = 50 W/m^2.

FA4) do not possess the highest photoactivity, which is in contrary to the common belief that anatase is the most active polymorph of titania.

The quantity and type of generated by-products during the experiments with different MEK concentrations are demonstrated in Fig. 13. Expectedly, when the inlet concentration is higher a greater number of MEK molecules are decomposed or partially oxidized and thus more by-products are produced. Considering the top graph in Fig. 13, the lowest health-hazards are obtained over H-SA2 for two reasons: small MEK degradation and large surface area, both of which contribute to lower HRI values. H-SA2 216.1 m^2/g surface area offers ample adsorption/ active sites which can host incoming MEK molecules as well as the by-

products generated throughout the PCO process. On the other hand, properly interconnected pores not only ease the diffusion of by-products (and MEK) into H-SA2 interiors, but act as trap and prevent the reintroduction of by-products (or intermediates) back to the gas phase. H-A10 and H-NA4 produce the largest quantities of by-products which is logical considering that they possess the highest removal efficiencies. It is interesting to note that although P25 has the second lowest MEK removal efficiency, it generates/releases a considerable amount of by-products. P25 small surface area in comparison to other titania samples brings about a severe adsorption competition among MEK, by-products, and water molecules. Therefore, light by-products such as acetone and
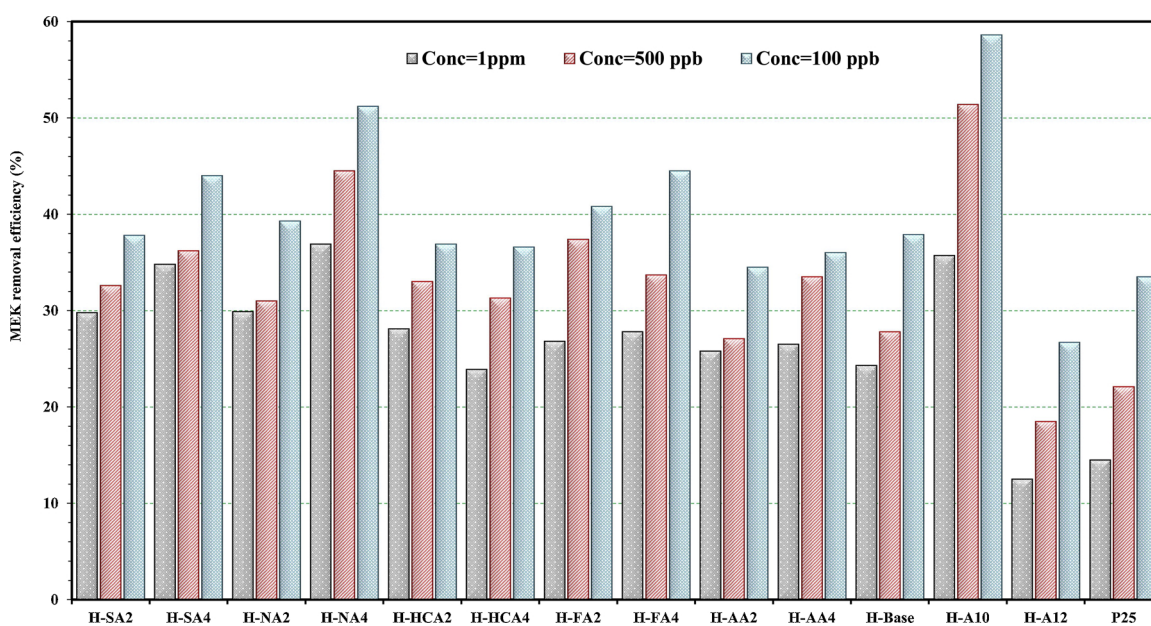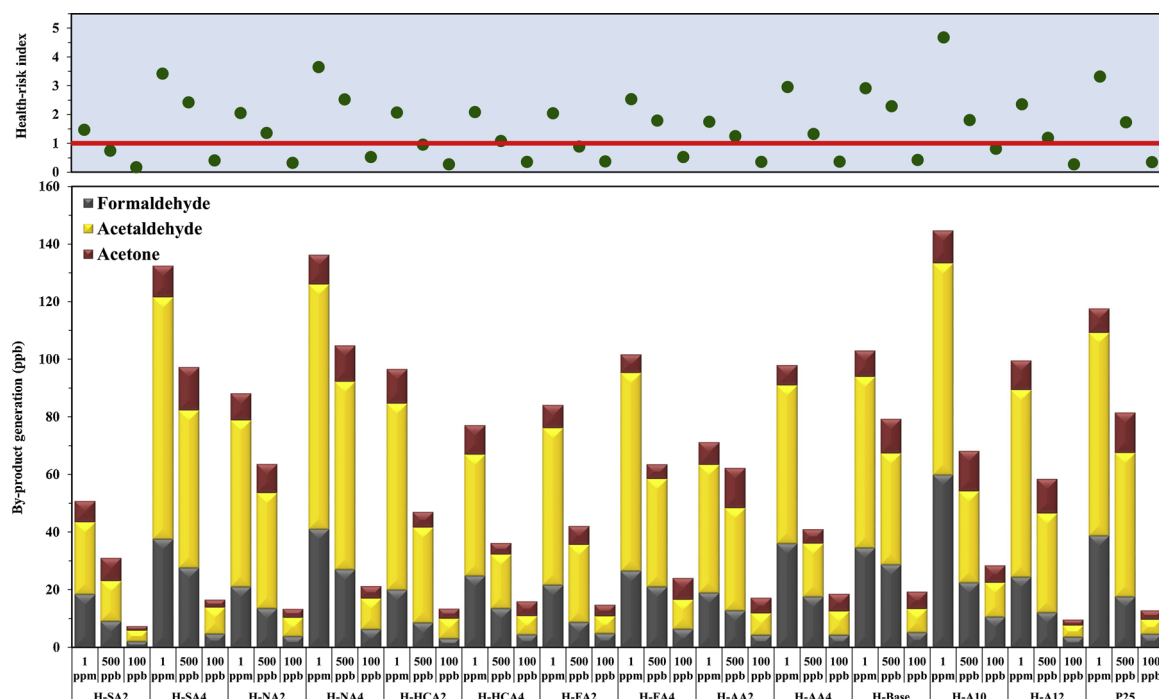

Fig. 12. Effect of inlet concentration on MEK removal efficiency over various photocatalysts. Relative humidity = 50%, residence time = 0.012 s, light intensity = 50 W/m^2.

Fig. 13. Effect of inlet concentration on by-products generation during MEK photocatalytic degradation. Relative humidity = 50%, residence time = 0.012 s, light intensity = 50 W/m^2.

formaldehyde are desorbed from the surface before undergoing the oxidation reactions toward complete mineralization. It has been suggested that the HRI value should not exceed 1 in order to assure a safe photocatalytic air purification system. As can be noted from the top graph in Fig. 13, in most cases where the inlet concentration is 100 or 500 ppb, HRI is smaller or very close to one. Consequently, if we consider the application of these PCO systems under actual operating conditions, the generated by-products will not pose serious health issues.

3.2.4. MEK degradation pathway

Based on the detected compounds in the gas-phase in this work and the intermediates/by-products reported in literature [64,69–72], a possible reaction pathway for photocatalytic oxidation of MEK is developed (Fig. 14). In step I, illumination of titanium dioxide leads to creation of electrons and holes, which subsequently react with water, oxygen, and OH groups on the surface and generate strong oxidants. MEK molecules react with the photogenerated positive holes and/or ·OHs to form alkyl radicals (H-abstraction). Through C-C scissions (step II) alkyl radicals break down into smaller alkyl radicals and various organic compounds including ketenes, ketones, propionaldehyde and propionic acid. Further surface reactions and radicals recombination result in the formation of ethanol, acetaldehyde, methanol and acetic acid. It has been suggested that during beta scissions several alkanes and alkenes might be produced (step IV) although not detected in the gas phase [72]. Besides its direct formation in step III, acetaldehyde can also be formed via oxidation of ethanol. Then, acetaldehyde itself is oxidized to formaldehyde, acetic acid and methanol. A major portion of these light compounds go through further oxidation reactions and eventually are converted to CO$_2$ and water.

4. Conclusions

Macro-/mesoporous hierarchical titanium dioxide photocatalysts were successfully synthesized, without employing any templates, using various acidic/basic hydrothermal media. The key characteristics of photocatalysts including crystallinity, surface area, crystal size, OH population, and porosity could be tailored by varying the pH of hydrothermal solution or the acid type. As general trends, crystallinity, crystal size, and e$^-$-h$^+$ separation efficiency improved with the pH of aqueous solution while surface area, mesoporosity, surface OH density, and brookite content declined. Formation of anatase and brookite phases under mildly acidic and basic hydrothermal environments was justified by Ostwald step rule, arrangements of TiO$_6$ octahedra in different phases, and titania surface protonation. The ability of acids to form anatase phase followed the sequence of formic > sulfuric > acetic > nitric ~ chloric. N$_2$ sorption showed that the pore size distribution widens as the alkalinity of reaction medium raises: 3.5–13 nm for H-SA2, 5–17 nm for H-Base, and 7–26 nm for H-A12. The direct observations in SEM and TEM along with the micro- and mesoporosity deduced from N$_2$ sorption analysis confirm porosity at different length scales. Regarding the impact of operating parameters, it was seen that an increment in the inlet concentration of MEK or airflow rate drastically decreases the removal efficiency mainly due to the limited adsorption of pollutant molecules onto the catalytic bed. In the case of relative humidity, for the large-surface-area and porous titania samples, the impact of humidity was marginal and always inhibiting due to the adsorption competition among MEK, intermediates, and water molecules over active sites. For samples with small surface area and P25, the removal efficiency peaked at relative humidity of 20%. In this study, we showed that it is possible to considerably enhance the photocatalytic performance by adjusting the key characteristics of titania during preparation stage. Variations in several properties follow opposite trends (e.g. surface area and crystallinity); therefore, it is of great importance to find the best balance between surface area, crystal size, crystallinity, OH density, and mesoporosity to optimize the photoactivity. Most of the developed photocatalysts reached health-risk indexes below or close to one under actual operating conditions, meaning we have a reliable and safe air purification system.
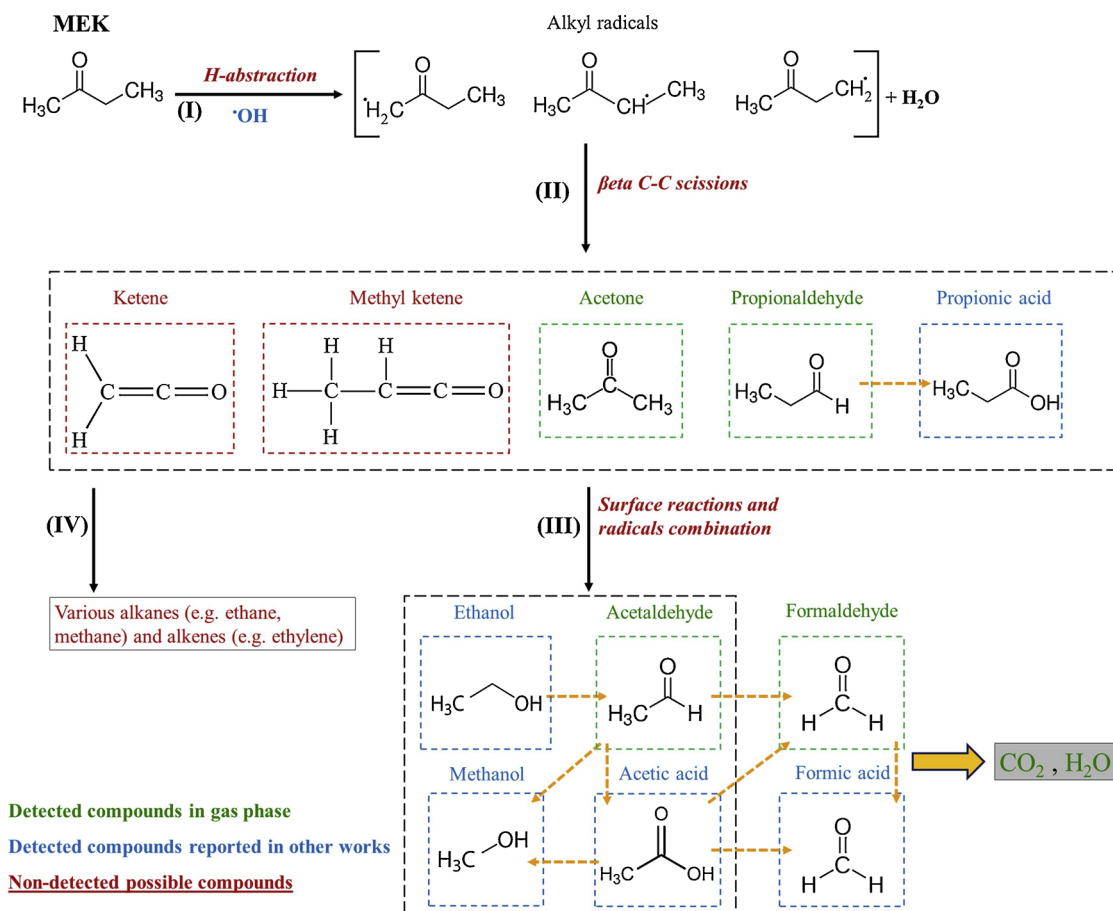
Fig. 14. Possible reaction pathway for photocatalytic oxidation of MEK over titanium dioxide.

Appendix A. Supplementary data

Supplementary material related to this article can be found, in the online version, at doi:https://doi.org/10.1016/j.apcatb.2019.03.057.

References

[1] A.H. Mamaghani, F. Haghighat, C.-S. Lee, Photocatalytic oxidation technology for indoor environment air purification: The state-of-the-art, Appl. Catal. B: Environ. 203 (2017) 247–269.

[2] Z. Shayegan, C.-S. Lee, F. Haghighat, TiO2 photocatalyst for removal of volatile organic compounds in gas phase – A review, Chem. Eng. J. 334 (2018) 2408–2439.

[3] M. Pelaez, N.T. Nolan, S.C. Pillai, M.K. Seery, P. Falaras, A.G. Kontos, P.S.M. Dunlop, J.W.J. Hamilton, J.A. Byrne, K. O'Shea, M.H. Entezari, D.D. Dionysiou, A review on the visible light active titanium dioxide photocatalysts for environmental applications, Appl. Catal. B: Environ. 125 (2012) 331–349.

[4] C. Raillard, V. Héquet, P.L. Cloirec, J. Legrand, TiO2 coating types influencing the role of water vapor on the photocatalytic oxidation of methyl ethyl ketone in the gas phase, Appl. Catal. B: Environ. 59 (2005) 213–220.

[5] J. Mo, Y. Zhang, Q. Xu, Effect of water vapor on the by-products and decomposition rate of ppb-level toluene by photocatalytic oxidation, Appl. Catal. B: Environ. 132-133 (2013) 212–218.

[6] A. Diamantopoulou, E. Sakellis, G.E. Romanos, S. Gardelis, N. Ioannidis, N. Boukos, P. Falaras, V. Likodimos, Titania photonic crystal photocatalysts functionalized by graphene oxide nanocolloids, Appl. Catal. B: Environ. 240 (2019) 277–290.

[7] W.H.M. Abdelraheem, M.K. Patil, M.N. Nadagouda, D.D. Dionysiou, Hydrothermal synthesis of photoactive nitrogen- and boron- codoped TiO2 nanoparticles for the treatment of bisphenol A in wastewater: synthesis, photocatalytic activity, degradation byproducts and reaction pathways, Appl. Catal. B: Environ. 241 (2019) 598–611.

[8] M.N. Lyulyukin, P.A. Kolinko, D.S. Selishchev, D.V. Kozlov, Hygienic aspects of TiO2-mediated photocatalytic oxidation of volatile organic compounds: air purification analysis using a total hazard index, Appl. Catal. B: Environ. 220 (2018) 386–396.

[9] X. Chen, S.S. Mao, Titanium dioxide nanomaterials: synthesis, properties, modifications, and applications, Chem. Rev. 107 (2007) 2891–2959.

[10] A.A. Ismail, D.W. Bahnemann, Mesoporous titania photocatalysts: preparation, characterization and reaction mechanisms, J. Mater. Chem. 21 (2011) 11686–11707.

[11] Y. Wang, Y. He, Q. Lai, M. Fan, Review of the progress in preparing nano TiO2: an important environmental engineering material, J. Environ. Sci. 26 (2014) 2139–2177.

[12] K. Byrappa, T. Adschiri, Hydrothermal technology for nanotechnology, Prog. Cryst. Growth Charact. Mater. 53 (2007) 117–166.

[13] X. Li, J. Yu, M. Jaroniec, Hierarchical photocatalysts, Chem. Soc. Rev. 45 (2016) 2603–2636.

[14] E. Grabowska, M. Marchelek, T. Klimczuk, G. Trykowski, A. Zaleska-Medynska, Noble metal modified TiO2 microspheres: surface properties and photocatalytic activity under UV–vis and visible light, J. Mol. Catal. A Chem. 423 (2016) 191–206.

[15] W. Schwieger, A.G. Machoke, T. Weissenberger, A. Inayat, T. Selvam, M. Klumpp, A. Inayat, Hierarchy concepts: classification and preparation strategies for zeolite containing materials with hierarchical porosity, Chem. Soc. Rev. 45 (2016) 3353–3376.

[16] X.-Y. Yang, A. Léonard, A. Lemaire, G. Tian, B.-L. Su, Self-formation phenomenon to hierarchically structured porous materials: design, synthesis, formation mechanism and applications, Chem. Commun. 47 (2011) 2763–2786.

[17] N.D. Petkovich, A. Stein, Controlling macro- and mesostructures with hierarchical porosity through combined hard and soft templating, Chem. Soc. Rev. 42 (2013) 3721–3739.

[18] Y. Liu, J. Goebl, Y. Yin, Templated synthesis of nanostructured materials, Chem. Soc. Rev. 42 (2013) 2610–2653.

[19] A. Collins, D. Carriazo, S.A. Davis, S. Mann, Spontaneous template-free assembly of ordered macroporous titania, Chem. Commun. (2004) 568–569.

[20] Q. Zhang, W. Wang, J. Goebl, Y. Yin, Self-templated synthesis of hollow nanostructures, Nano Today 4 (2009) 494–507.

[21] C. Raillard, V. Héquet, P. Le Cloirec, J. Legrand, Comparison of different TiO2 photocatalysts for the gas phase oxidation of volatile organic compounds, Water Sci. Technol. 50 (2004) 241–250.

[22] A. Alonso-Tellez, R. Masson, D. Robert, N. Keller, V. Keller, Comparison of Hombikat UV100 and P25 TiO2 performance in gas-phase photocatalytic oxidation

reactions, J. Photochem. Photobiol. A Chem. 250 (2012) 58–65.

[23] A. Motamed Dashliborun, R. Sotudeh-Gharebagh, M. Hajaghazadeh, H. Kakooei, S. Afshar, Modeling of the photocatalytic degradation of methyl ethyl ketone in a fluidized bed reactor of nano-TiO2/γ-Al2O3 particles, Chem. Eng. J. 226 (2013) 59–67.

[24] Y. Yan, V. Keller, N. Keller, On the role of BmimPF6 and P/F- containing additives in the sol-gel synthesis of TiO2 photocatalysts with enhanced activity in the gas phase degradation of methyl ethyl ketone, Appl. Catal. B: Environ. 234 (2018) 56–69.

[25] L.A. Diniz, T.L.R. Hewer, D. Matsumoto, A.C.S.C. Teixeira, A comparison between the four Geldart groups on the performance of a gas-phase annular fluidized bed photoreactor for volatile organic compound oxidation, Environ. Sci. Pollut. Res. 26 (2019) 4242–4252.

[26] R.A.R. Monteiro, F.V.S. Lopes, R.A.R. Boaventura, A.M.T. Silva, V.J.P. Vilar, Synthesis and characterization of N-modified titania nanotubes for photocatalytic applications, Environ. Sci. Pollut. Res. 22 (2015) 810–819.

[27] N. Arconada, Y. Castro, A. Durán, V. Héquet, Photocatalytic oxidation of methyl ethyl ketones over sol–gel mesoporous and meso-structured TiO2 films obtained by EISA method, Appl. Catal. B: Environ. 107 (2011) 52–58.

[28] M. Hajaghazadeh, V. Vaiano, D. Sannino, H. Kakooei, R. Sotudeh-Gharebagh, P. Ciambelli, Heterogeneous photocatalytic oxidation of methyl ethyl ketone under UV-A light in an LED-fluidized bed reactor, Catal. Today 230 (2014) 79–84.

[29] P.-T. Hsiao, M.-D. Lu, Y.-L. Tung, H. Teng, Influence of hydrothermal pressure during crystallization on the structure and electron-conveying ability of TiO2 colloids for dye-sensitized solar cells, J. Phys. Chem. C 114 (2010) 15625–15632.

[30] S. NIOSH, National Institute for Occupational Safety and Health (NIOSH), (2018) http://www.cdc.gov/niosh/.

[31] J. Yu, J.C. Yu, M.K.P. Leung, W. Ho, B. Cheng, X. Zhao, J. Zhao, Effects of acidic and basic hydrolysis catalysts on the photocatalytic activity and microstructures of bimodal mesoporous titania, J. Catal. 217 (2003) 69–78.

[32] K. Chen, L. Zhu, K. Yang, Acid-assisted hydrothermal synthesis of nanocrystalline TiO2 from titanate nanotubes: influence of acids on the photodegradation of gaseous toluene, J. Environ. Sci. 27 (2015) 232–240.

[33] K. Xia, D. Ferguson, Y. Djaoued, J. Robichaud, N. Tchoukanova, R. Brüning, E. McCalla, Template-free synthesis and photocatalytic activity of hierarchical porous titania with controlled texture and crystalline structure, Appl. Catal. A: Gen. 387 (2010) 231–241.

[34] N.M. Kinsinger, A. Wong, D. Li, F. Villalobos, D. Kisailus, Nucleation and crystal growth of nanocrystalline anatase and rutile phase TiO2 from a water-soluble precursor, Cryst. Growth Des. 10 (2010) 5254–5261.

[35] T.-D. Nguyen Phan, H.-D. Pham, T. Viet Cuong, E. Jung Kim, S. Kim, E. Woo Shin, A simple hydrothermal preparation of TiO2 nanomaterials using concentrated hydrochloric acid, J. Cryst. Growth 312 (2009) 79–85.

[36] D. Bahnemann, A. Henglein, L. Spanhel, Detection of the intermediates of colloidal TiO2-catalysed photoreactions, Faraday Discuss. Chem. Soc. 78 (1984) 151–163.

[37] H. Yin, Y. Wada, T. Kitamura, S. Kambe, S. Murasawa, H. Mori, T. Sakata, S. Yanagida, Hydrothermal synthesis of nanosized anatase and rutile TiO2 using amorphous phase TiO2, J. Mater. Chem. 11 (2001) 1694–1703.

[38] W.S. Nam, G.Y. Han, A photocatalytic performance of TiO2 photocatalyst prepared by the hydrothermal method, Korean J. Chem. Eng. 20 (2003) 180–184.

[39] Z. Wang, D. Xia, G. Chen, T. Yang, Y. Chen, The effects of different acids on the preparation of TiO2 nanostructure in liquid media at low temperature, Mater. Chem. Phys. 111 (2008) 313–316.

[40] H. Zhang, J.F. Banfield, Understanding polymorphic phase transformation behavior during growth of nanocrystalline aggregates: insights from TiO2, J. Phys. Chem. B 104 (2000) 3481–3487.

[41] J. Yu, Y. Su, B. Cheng, M. Zhou, Effects of pH on the microstructures and photocatalytic activity of mesoporous nanocrystalline titania powders prepared via hydrothermal method, J. Mol. Catal. A Chem. 258 (2006) 104–112.

[42] A. Pottier, S. Cassaignon, C. Chanéac, F. Villain, E. Tronc, J.-P. Jolivet, Size tailoring of TiO2 anatase nanoparticles in aqueous medium and synthesis of nanocomposites. Characterization by Raman spectroscopy, J. Mater. Chem. 13 (2003) 877–882.

[43] Z. Wu, Z. Gu, W. Zhao, H. Wang, Photocatalytic oxidation of gaseous benzene over nanosized TiO2 prepared by solvothermal method, Chin. Sci. Bull. 52 (2007) 3061–3067.

[44] W.F. Zhang, M.S. Zhang, Z. Yin, Q. Chen, Photoluminescence in anatase titanium dioxide nanocrystals, Appl. Phys. B 70 (2000) 261–265.

[45] Q. Xiang, K. Lv, J. Yu, Pivotal role of fluorine in enhanced photocatalytic activity of anatase TiO2 nanosheets with dominant (001) facets for the photocatalytic degradation of acetone in air, Appl. Catal. B: Environ. 96 (2010) 557–564.

[46] S.T. Nishanthi, S. Iyyapushpam, B. Sundarakannan, E. Subramanian, D. Pathinettam Padiyan, Inter-relationship between extent of anatase crystalline phase and photocatalytic activity of TiO2 nanotubes prepared by anodization and annealing method, Sep. Purif. Technol. 131 (2014) 102–107.

[47] H. Tang, H. Berger, P.E. Schmid, F. Lévy, G. Burri, Photoluminescence in TiO2 anatase single crystals, Solid State Commun. 87 (1993) 847–850.

[48] J. Kaur, R. Singh, B. Pal, Influence of coinage and platinum group metal co-catalysis

for the photocatalytic reduction of m-dinitrobenzene by P25 and rutile TiO2, J. Mol. Catal. A Chem. 397 (2015) 99–105.

[49] J. Araña, A.P. Alonso, J.M.D. Rodríguez, G. Colón, J.A. Navío, J.P. Peña, FTIR study of photocatalytic degradation of 2-propanol in gas phase with different TiO2 catalysts, Appl. Catal. B: Environ. 89 (2009) 204–213.

[50] J. Yu, T. Ma, S. Liu, Enhanced photocatalytic activity of mesoporous TiO2 aggregates by embedding carbon nanotubes as electron-transfer channel, Phys. Chem. Chem. Phys. 13 (2011) 3491–3501.

[51] Z. He, Z. Zhu, J. Li, J. Zhou, N. Wei, Characterization and activity of mesoporous titanium dioxide beads with high surface areas and controllable pore sizes, J. Hazard. Mater. 190 (2011) 133–139.

[52] Y. Qiu, X. Li, Synthesis of peroxo-titanium decorated H-titanate-nanotube-based hierarchical microspheres with enhanced visible-light photocatalytic activity in degradation of Rhodamine B, Dalton Trans. 43 (2014) 14537–14541.

[53] B. Lindberg, R. Maripuu, K. Siegbahn, R. Larsson, C.G. Gölander, J.C. Eriksson, ESCA studies of heparinized and related surfaces: 1. Model surfaces on steel substrates, J. Colloid Interface Science 95 (1983) 308–321.

[54] Y. Shuang, Y. Hou, B. Zhang, H.G. Yang, Impurity-Free synthesis of cube-like single-crystal anatase TiO2 for High performance dye-sensitized solar cell, Ind. Eng. Chem. Res. 52 (2013) 4098–4102.

[55] S. Liu, C. Liu, W. Wang, B. Cheng, J. Yu, Unique photocatalytic oxidation reactivity and selectivity of TiO2–graphene nanocomposites, Nanoscale 4 (2012) 3193–3200.

[56] M. Diak, M. Klein, T. Klimczuk, W. Lisowski, H. Remita, A. Zaleska-Medynska, E. Grabowska, Photoactivity of decahedral TiO2 loaded with bimetallic nanoparticles: degradation pathway of phenol-1-13C and hydroxyl radical formation, Appl. Catal. B: Environ. 200 (2017) 56–71.

[57] C.-R. Ke, L.-C. Chen, J.-M. Ting, Photoanodes consisting of mesoporous anatase TiO2 beads with various sizes for High-efficiency flexible dye-sensitized solar cells, J. Phys. Chem. C 116 (2012) 2600–2607.

[58] L. Wu, Y. Qiu, M. Xi, X. Li, C. Cen, Fabrication of TiO2 nanotubes-assembled hierarchical microspheres with enhanced photocatalytic degradation activity, New J. Chem. 39 (2015) 4766–4773.

[59] H. Lin, J. Long, Q. Gu, W. Zhang, R. Ruan, Z. Li, X. Wang, In situ IR study of surface hydroxyl species of dehydrated TiO2: towards understanding pivotal surface processes of TiO2 photocatalytic oxidation of toluene, Phys. Chem. Chem. Phys. 14 (2012) 9468–9474.

[60] C. Deiana, E. Fois, S. Coluccia, G. Martra, Surface structure of TiO2 P25 nanoparticles: infrared study of hydroxy groups on coordinative defect sites, J. Phys. Chem. C 114 (2010) 21531–21538.

[61] A.H. Mamaghani, F. Haghighat, C.-S. Lee, Gas phase adsorption of volatile organic compounds onto titanium dioxide photocatalysts, Chem. Eng. J. 337 (2018) 60–73.

[62] M. Sleiman, P. Conchon, C. Ferronato, J.-M. Chovelon, Photocatalytic oxidation of toluene at indoor air levels (ppbv): towards a better assessment of conversion, reaction intermediates and mineralization, Appl. Catal. B: Environ. 86 (2009) 159–165.

[63] N. Bouazza, M.A. Lillo-Ródenas, A. Linares-Solano, Photocatalytic activity of TiO2-based materials for the oxidation of propene and benzene at low concentration in presence of humidity, Appl. Catal. B: Environ. 84 (2008) 691–698.

[64] A.H. Mamaghani, F. Haghighat, C.-S. Lee, Photocatalytic degradation of VOCs on various commercial titanium dioxides: impact of operating parameters on removal efficiency and by-products generation, Build. Environ. 138 (2018) 275–282.

[65] N. Quici, M.L. Vera, H. Choi, G.L. Puma, D.D. Dionysiou, M.I. Litter, H. Destaillats, Effect of key parameters on the photocatalytic oxidation of toluene at low concentrations in air under 254 + 185 nm UV irradiation, Appl. Catal. B: Environ. 95 (2010) 312–319.

[66] P. Pichat, Some views about indoor air photocatalytic treatment using TiO2: conceptualization of humidity effects, active oxygen species, problem of C1–C3 carbonyl pollutants, Appl. Catal. B: Environ. 99 (2010) 428–434.

[67] D. Vildozo, R. Portela, C. Ferronato, J.-M. Chovelon, Photocatalytic oxidation of 2-propanol/toluene binary mixtures at indoor air concentration levels, Appl. Catal. B: Environ. 107 (2011) 347–354.

[68] F.V.S. Lopes, R.A.R. Monteiro, A.M.T. Silva, G.V. Silva, J.L. Faria, A.M. Mendes, V.J.P. Vilar, R.A.R. Boaventura, Insights into UV-TiO2 photocatalytic degradation of PCE for air decontamination systems, Chem. Eng. J. 204–206 (2012) 244–257.

[69] L. Zhong, F. Haghighat, C.-S. Lee, N. Lakdawala, Performance of ultraviolet photocatalytic oxidation for indoor air applications: systematic experimental evaluation, J. Hazard. Mater. 261 (2013) 130–138.

[70] C. Raillard, V. Hequet, P. Le Cloirec, J. Legrand, Photocatalytic Oxidation of Methyl Ethyl Ketone Over Sol-Gel and Commercial TiO2 for the Improvement of Indoor Air, (2006).

[71] T. Machold, W.Y. Suprun, H. Papp, Characterization of VOx-TiO2 catalysts and their activity in the partial oxidation of methyl ethyl ketone, J. Mol. Catal. A Chem. 280 (2008) 122–130.

[72] G. Vincent, A. Queffeulou, P.M. Marquaire, O. Zahraa, Remediation of olfactory pollution by photocatalytic degradation process: study of methyl ethyl ketone (MEK), J. Photochem. Photobiol. A Chem. 191 (2007) 42–50.